*J. Fluid Mech.* (2002), *vol.* 457, *pp.* 79–109.  
DOI: 10.1017/S0022112001007595 Printed in the United Kingdom

# Planimetric instability of channels with variable width

By R. REPETTO[1], M. TUBINO[2] AND C. PAOLA[3]

[1]Dipartimento di Ingegneria delle Strutture, delle Acque e del Terreno, Università dell'Aquila, Monteluco di Roio, 67040, L'Aquila, Italy

[2]Dipartimento di Ingegneria Civile e Ambientale, Università di Trento, Via Mesiano 77, 38050, Trento, Italy

[3]St Anthony Falls Laboratory, University of Minnesota, 3rd Avenue SE and Mississippi River, Minneapolis, MN 55414, USA

(Received 12 January 2001 and in revised form 17 August 2001)

We study the steady three-dimensional flow field and bed topography in a channel with sinusoidally varying width, under the assumptions of small-amplitude width variations and sufficiently wide channel to neglect nonlinear effects and sidewall effects. The aim of the work is to investigate the role of width variations in producing channel bifurcation in braided rivers. We infer incipient bifurcation in cases where the growth of a central bar leads to planimetric instability of the channel, i.e. when the given infinitesimal width perturbation is enhanced. Results of the three-dimensional model suggest that the equilibrium bottom profile mainly consists of a purely longitudinal component, uniformly distributed over the cross-section, which induces deposition at the wide section and scour at the constriction, and of a transverse component in the form of a central bar (wide sections) and scour (constrictions), with longitudinal wavelength equal to that of width variations. A comparison between the results of the three-dimensional model and those obtained by means of a two-dimensional depth-averaged approach shows that the transverse component is mainly related to three-dimensional effects. Theoretical findings display a satisfactory agreement with results of flume experiments. Transverse variations are responsible for the planimetric instability of the channel; we find that in the range of values of Shields stress typical of braided rivers, the incipient bifurcation is enhanced as the width ratio of the channel increases.

## 1. Introduction

The morphological behaviour of movable bed rivers is essentially governed by the interaction between free bedforms, spontaneously developing in the channel as the result of an inherent instability of the flow-erodible bed system, and forced bedforms produced by physical constraints, such as curvature, width variations, backwater effects, etc. (Seminara & Tubino 1989; Seminara 1995). In many cases it has been observed that, provided the forcing effect is large enough, freely migrating forms are suppressed in favour of a steady bottom pattern which in turn may affect the planimetrical channel behaviour.

The case of planimetric forcing produced by channel curvature has received much attention (Kinoshita & Miwa 1974; Shimizu & Itakura 1989; Tubino & Seminara 1990; Whiting & Dietrich 1993), because of its natural association with the development of river meanders. In the same way that curvature-forced bars can be seen

FIGURE 1. Thjorsa river, Iceland.

as the 'molecules' of meandering rivers, a couplet consisting of a channel narrowing with deep central scour leading downstream to a widened section with a central bar has been proposed as the 'molecule' of braided rivers (Mosley 1976). A braided river comprises a network of interlaced channels (figure 1) which display a significant variation in width, both of the individual channel segments and of the whole channel ensemble. These width variations seem to be associated with bank erosion, bar development and channel curvature. Furthermore, width variations appear to be crucial in understanding the bifurcation mechanism that leads to production of new channels in braided rivers. Although the conditions under which a channel bifurcates have yet to be understood in detail, it seems indisputable that streamline divergence is one of the mechanisms leading to the division of a stream, as suggested by field observations and flume experiments. Leopold & Wolman (1957) pointed out that channel bifurcation is typically the consequence of streamline divergence due to the presence of a steady bar. Ashmore (1982, 1991) has experimentally investigated in detail the possible mechanisms of braiding generation starting from a straight, laterally unconstrained, cohesionless channel. Typically, the generation of alternate bars was observed at the initial stage of each run (figure 2), which induced a weak curvature of the stream. Furthermore, the development of bar pools provided preferential sites for bank erosion, leading to a sequence of bumps along both banks. As a response to this planform, width variations formed, displaying a wavelength equal to half the wavelength of curvature distribution. Under such conditions migrating alternate bars were transformed into a steady bar pattern. The resulting bed topography and flow field were often likely to enhance the amplitude of width variations, leading to the bifurcation of the channel which mainly arose from chute cutting across the initial bars.

Despite this evidence of the effect of width variations in shaping bed topography, it has been neglected in most theoretical treatments of river morphodynamics (but see Bittner 1994). The present work is aimed at investigating the role of width variation in producing planform instability. We focus particularly on the formation of central bars and their role in producing channel divisions. We consider the simple

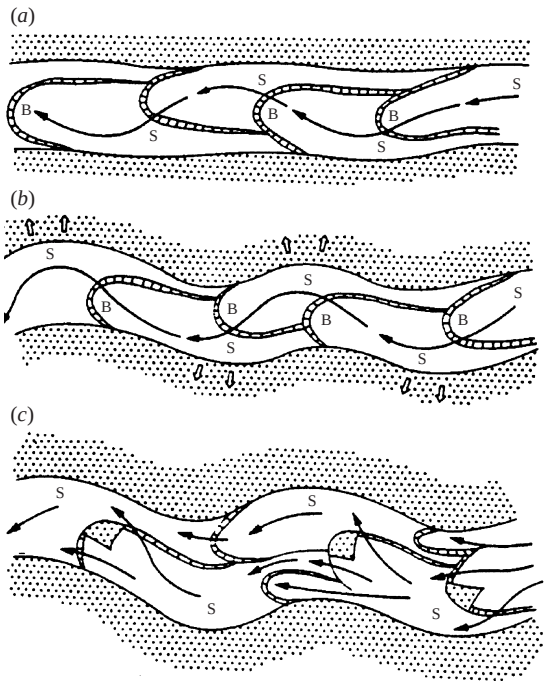


FIGURE 2. Channel evolution and generation of a bifurcation (Ashmore 1982).

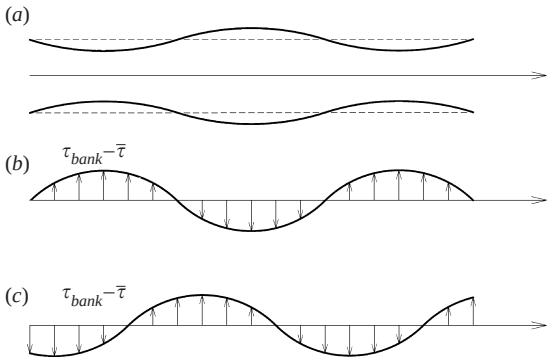


FIGURE 3. (*a*) Sketch of channel geometry. Stress distribution under (*b*) stable and (*c*) unstable conditions ($\overline{\tau}$ is the cross-sectionally averaged bottom stress).

geometry sketched in figure 3(*a*) consisting of a straight, infinitely long channel with vertical banks, subject to periodic width variations of small amplitude. This idealized configuration can be considered as representing the main component of a spectral analysis of width distribution of a real river. We study the flow field and bed topography induced by the forcing effect of non-uniform geometry, assuming mobile bed and fixed sidewalls. We then investigate the conditions under which the channel is planimetrically stable or unstable, i.e. it tends to damp or enhance the given initial small perturbation of width. Bank stability is analysed through a simplified approach, relating the rate of bank retreat to the excess depth-averaged velocity at the bank induced by flow perturbations which arise as a consequence of width variations; in other words, we assume that the channel would be stable without the forcing effect of

variable width. Notice that in the present work, bank erosion is assumed to be slow with respect to bottom evolution, thus justifying the assumption that, on the time scale of flow and bed development, the planimetric configuration is assumed to be steady. The latter hypothesis may turn out to be inadequate when applied to single branches of rivers with non-cohesive banks, for which bed and bank development may have similar time scales. Therefore, the present work is aimed at predicting the tendency of planform evolution, without the claim to describe its time development.

Following the above line of reasoning, a one-dimensional approach to the problem would necessarily lead to a stable configuration (figure 3*b*), with an excess of velocity at the narrow sections and a deficit of velocity at the wide sections. Under these conditions, the flow tends to widen the narrowest part of the channel until a constant width configuration is eventually reestablished.

In the present paper, both a two-dimensional and a three-dimensional model are proposed. If we consider the cross-sectionally averaged velocities, these models must obviously reproduce the results of the simpler one-dimensional approach. However, they allow the possibility of transverse variations in each cross-section so that, even though the cross-sectionally averaged velocity attains its maximum close to the narrowest section, it is possible that the actual velocity at the bank peaks where the channel is still wider than the average (figure 3*c*). In this situation, the planform is unstable as bank erosion tends to enhance the initially small width perturbation. The above speculations suggest that the eventual planimetric instability of the channel, and the consequent generation of a bifurcation, are inherently associated with strong transverse variations of flow and bed characteristics.

The rest of the paper is organized as follows. In § 2, we develop a two-dimensional model for the flow field and bed topography in a channel with sinusoidally varying width. The three-dimensional version of the model is introduced in § 3. Section 4 is devoted to the description of experiments performed in a mobile bed flume in the Hydraulic Laboratory of Trento University. A comparison between experimental results and theoretical predictions of bed topography is reported in § 5. In § 6, we show how the predictions based on the two-dimensional approach can be improved by taking into account the effect of streamline curvature. Planimetric instability of channels with variable width is discussed in § 7. Finally, we make some concluding remarks in § 8.

## 2. Two-dimensional depth-averaged model

### 2.1. *Formulation of the problem*

We consider the flow in a straight cohesionless channel, with average width $2b_0^*$ over which small-amplitude sinusoidal variations are superimposed. Hence, the sidewalls of the channel are described by the following equation:

$$y^* = \pm b^* = \pm b_0^*[1 + \delta(\exp(\mathrm{i}\lambda_b^* x^*) + \text{c.c.})], \quad \lambda_b^* = \frac{2\pi}{L_b^*}, \quad \delta \ll 1, \tag{2.1a–c}$$

where $L_b^*$ is the wavelength of width variations. Furthermore, c.c. denotes the complex conjugate and $x^*$ and $y^*$ are longitudinal and transverse coordinates (the superscript asterisks indicate dimensional variables that will be made dimensionless below).

As a first step, we tackle the problem within the context of a two-dimensional depth-averaged flow model.

We stretch our physical domain into a rectangle normalizing the transverse coor-

dinate $y^*$ with the local width in the form

$$y = \frac{y^*}{b^*(x^*)}, \tag{2.2}$$

so that $y$ falls in the range $(-1, 1)$. Furthermore, let us define dimensionless variables as follows

$$(x^*, b^*) = b_0^*(x, b), \quad \boldsymbol{U}^* = U_0^* \boldsymbol{U}, \quad (H^*, D^*) = D_0^*(H, D), \tag{2.3a–c}$$

$$\lambda_b^* = \frac{\lambda_b}{b_0^*} \quad \boldsymbol{\tau}^* = \rho U_0^{*2} \boldsymbol{\tau}, \quad \boldsymbol{q}^* = d_s^* \sqrt{\frac{\rho_s - \rho}{\rho} g d_s^*}\, \boldsymbol{q}, \tag{2.3d–f}$$

where $\boldsymbol{U}^* = (U^*, V^*)$ is the velocity vector, $H^*$ is the water level, $D^*$ is the water depth, $\boldsymbol{\tau}^* = (\tau_x^*, \tau_y^*)$ is the bottom stress vector, $\boldsymbol{q}^* = (q_x^*, q_y^*)$ is the sediment transport vector per unit width, $\rho$ is the water density and $g$ is the acceleration due to gravity. Furthermore, $\rho_s$ and $d_s^*$ are sediment density and diameter, respectively, and $U_0^*$ and $D_0^*$ are average speed and depth of a reference uniform flow in the channel with constant width $2b_0^*$, for given water discharge, slope and grain size. The assumption of constant grain size may appear to be rather crude when applied to gravel bed rivers. Theoretical and experimental works have investigated the role of sorting in the development of gravel bed rivers suggesting that its effect is not overwhelming unless close to critical conditions for sediment motion. In this respect the present work has to be considered as a first attempt to model the evolution of a channel in braided networks to which the complicating effect of sediment sorting may be added later.

Notice that we look for the steady configuration induced by width variations, hence time derivatives are neglected in flow equations and sediment continuity equation. Using the above scales and the coordinate transformation (2.2), flow equations and sediment continuity equation then take the following dimensionless form:

$$bUU_{,x} + VU_{,y} + b\frac{H_{,x}}{F_0^2} + b\frac{\beta\tau_x}{D} - yb_{,x}UU_{,y} - yb_{,x}\frac{H_{,y}}{F_0^2} = 0, \tag{2.4a}$$

$$bUV_{,x} + VV_{,y} + \frac{H_{,y}}{F_0^2} + b\frac{\beta\tau_y}{D} - yb_{,x}UV_{,y} = 0, \tag{2.4b}$$

$$b(UD)_{,x} + (VD)_{,y} - yb_{,x}(UD)_{,y} = 0, \tag{2.4c}$$

$$bq_{x,x} + q_{y,y} - yb_{,x}q_{x,y} = 0, \tag{2.4d}$$

where

$$\beta = \frac{b_0^*}{D_0^*} \tag{2.5}$$

is the average aspect ratio of the channel and $F_0$ is the Froude number of the reference uniform flow.

The boundary conditions impose the physical requirement that channel walls be impermeable both to flow and to sediment transport; in dimensionless form they read

$$\boldsymbol{U} \cdot \hat{\boldsymbol{n}}_b = -Ub_{,x} \pm V = 0 \quad (y = \pm 1), \tag{2.6a}$$

$$\boldsymbol{q} \cdot \hat{\boldsymbol{n}}_b = -q_x b_{,x} \pm q_y = 0 \quad (y = \pm 1). \tag{2.6b}$$

where $\hat{\boldsymbol{n}}_b$ is the unit vector normal to the banks. Notice that the effect of width variations is felt through the dependence on the shape of the banks embodied in the definition of the unit vector appearing in the boundary conditions (2.6$a$, $b$).

In order to close the mathematical problem we write the shear stress components in terms of a friction coefficient $C_f$ in the form

$$(\tau_x, \tau_y) = (U, V)(U^2 + V^2)^{1/2} C_f, \tag{2.7}$$

where

$$C_f^{-1/2} = 6 + 2.5 \ln\left(\frac{D}{2.5 d_s}\right), \quad d_s = \frac{d_s^*}{D_0^*}. \tag{2.8a,b}$$

Furthermore, we assume the sediment to be mainly transported as bedload. Hence, the present theory should work best in the field for gravel bed rivers. Bedload intensity $\Phi$ is evaluated through the Parker (1990) formula in terms of the local value of the Shields parameter

$$\vartheta = \frac{|\boldsymbol{\tau}^*|}{(\rho_s - \rho) g d_s^*}. \tag{2.9}$$

The local bed slope modifies the direction of the bedload. The effect can be quantified on the basis of experimental observations (Ikeda 1982; Talmon, Struiksma & Van Mierlo 1995) which suggest the following estimate for the angle $\phi$ describing the deviation of particle trajectories with respect to the local bed stress vector

$$\tan(\phi) = -\frac{r}{\beta\sqrt{\vartheta}} G, \tag{2.10}$$

where $r$ is an empirical coefficient ranging between 0.3 and 1 and $G$ is the local bottom gradient normal to the bed stress vector. Hence, the bedload components are

$$\boldsymbol{q} = \frac{\Phi}{|\boldsymbol{\tau}|}[\tau_x \cos(\phi) - \tau_y \sin(\phi), \tau_x \sin(\phi) + \tau_y \cos(\phi)]. \tag{2.11}$$

The above formula strictly applies to the case of a gently sloping bed. Braided rivers often display strong transverse and longitudinal bed gradients, hence a nonlinear modelling of the bed slope effect, like that proposed by Kovacs & Parker (1994) and recently revised by Parker, Seminara & Solari (2000), would be appropriate for modelling a fully developed topography. However, equations (2.10) and (2.11) are appropriate in the present linearized case.

### 2.2. *Linear solution*

The hypothesis of small-amplitude width variations, mathematically expressed by (2.1*c*), allows us to linearize the problem introducing the following expansion:

$$(U, V, H, D) = (1, 0, \bar{H}, 1) + \delta[\exp(\mathrm{i}\lambda_b x)(U_1, V_1, H_1, D_1) + \text{c.c.}] + O(\delta^2). \tag{2.12}$$

At order $O(\delta)$, the linearized form of equations (2.4*a–d*) is

$$a_1 U_1 + a_2 H_1 + a_3 D_1 = 0, \tag{2.13a}$$

$$a_4 V_1 + a_5 \frac{\mathrm{d}H_1}{\mathrm{d}y} = 0, \tag{2.13b}$$

$$a_6 U_1 + \frac{\mathrm{d}V_1}{\mathrm{d}y} + a_6 D_1 = 0, \tag{2.13c}$$

$$a_7 U_1 + a_8 \frac{\mathrm{d}V_1}{\mathrm{d}y} + a_9 \frac{\mathrm{d}^2(D_1 - H_1)}{\mathrm{d}y^2} + a_{10} D_1 = 0, \tag{2.13d}$$

where the coefficients are defined as follows:

$$\left.\begin{array}{lll} a_1 = \mathrm{i}\lambda_b + 2\beta C_{f0}, & a_2 = \mathrm{i}\lambda_b F_0^{-2}, & a_3 = \beta C_{f0}(C_D - 1), \\ a_4 = \mathrm{i}\lambda_b + \beta C_{f0}, & a_5 = F_0^{-2}, & a_6 = \mathrm{i}\lambda_b, \\ a_7 = 2\mathrm{i}\lambda_b \Phi_T, & a_8 = 1, & a_9 = \dfrac{r}{\beta\sqrt{\vartheta_0}}, \\ a_{10} = \mathrm{i}\lambda_b C_D \Phi_T, & & \end{array}\right\} \tag{2.14}$$

and

$$C_D = \left(\frac{1}{C_f}\frac{\mathrm{d}C_f}{\mathrm{d}D}\right)_{D=1} \qquad \Phi_T = \left(\frac{\vartheta}{\Phi}\frac{\mathrm{d}\Phi}{\mathrm{d}\vartheta}\right)_{\vartheta=\vartheta_0}. \tag{2.15a,b}$$

Finally, $\vartheta_0$ and $C_{f0}$ represent the Shields stress and the friction coefficient of the reference uniform flow.

The linearized form of the boundary conditions is obtained from (2.6*a*, *b*) and reads:

$$V_1 = \pm\mathrm{i}\lambda_b \quad (y = \pm 1), \tag{2.16a}$$

$$\frac{\mathrm{d}(H_1 - D_1)}{\mathrm{d}y} = 0 \quad (y = \pm 1). \tag{2.16b}$$

System (2.13*a–d*), with the boundary conditions (2.16*a*, *b*), leads to the following fourth-order ordinary problem for the variable $V_1$

$$\frac{\mathrm{d}^4 V_1}{\mathrm{d}y^4} + \Gamma_1 \frac{\mathrm{d}^2 V_1}{\mathrm{d}y^2} + \Gamma_2 V_1 = 0, \tag{2.17a}$$

$$V_1 = \pm\mathrm{i}\lambda_b \quad (y = \pm 1), \tag{2.17b}$$

$$\frac{\mathrm{d}^2 V_1}{\mathrm{d}y^2} = \pm\mathrm{i}\lambda_b \Gamma_3 \quad (y = \pm 1), \tag{2.17c}$$

where

$$\Gamma_1 = \frac{1}{a_1 a_9}\left[a_6(a_3 - a_1)\left(a_8 + \frac{a_4 a_9}{a_5}\right) - a_3 a_7 + a_1 a_{10} + a_2 a_4 a_6 a_9\right], \tag{2.18a}$$

$$\Gamma_2 = \frac{a_2 a_4 a_6}{a_1 a_5 a_9}(a_{10} - a_7), \tag{2.18b}$$

$$\Gamma_3 = -\frac{a_4 a_6}{a_1 a_5}(a_3 - a_1 + a_2). \tag{2.18c}$$

The analytical solution of the above problem can be readily obtained in the form

$$V_1 = \gamma_1 \sinh(\lambda_1 y) + \gamma_2 \sinh(\lambda_2 y), \tag{2.19}$$

where

$$\lambda_1 = \sqrt{\tfrac{1}{2}\left(-\Gamma_1 + \sqrt{\Gamma_1^2 - 4\Gamma_2}\right)}, \tag{2.20a}$$

$$\lambda_2 = \sqrt{\tfrac{1}{2}\left(-\Gamma_1 - \sqrt{\Gamma_1^2 - 4\Gamma_2}\right)}, \tag{2.20b}$$

and

$$\gamma_1 = \frac{\mathrm{i}\lambda_b(\lambda_2^2 - \Gamma_3)}{(\lambda_2^2 - \lambda_1^2)\sinh(\lambda_1)}, \quad \gamma_2 = \frac{\mathrm{i}\lambda_b(\lambda_1^2 - \Gamma_3)}{(\lambda_1^2 - \lambda_2^2)\sinh(\lambda_2)}. \tag{2.21a,b}$$

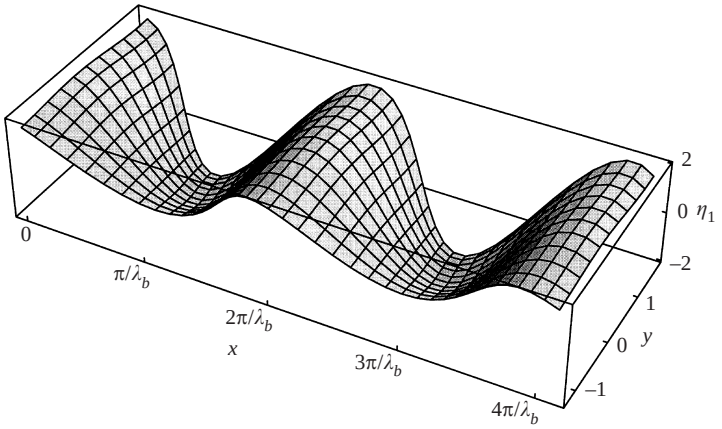


FIGURE 4. Two-dimensional model. Typical equilibrium bed configuration: $\lambda_b = 0.2$, $\beta = 15$, $\vartheta_0 = 0.07$, $d_s = 0.05$.

Integrating (2.13$b$) and using (2.13$a$) and (2.13$c$) we obtain

$$U_1 = \phi_1 \cosh(\lambda_1 y) + \phi_2 \cosh(\lambda_2 y), \tag{2.22a}$$

$$H_1 = \theta_1 \cosh(\lambda_1 y) + \theta_2 \cosh(\lambda_2 y), \tag{2.22b}$$

$$D_1 = \delta_1 \cosh(\lambda_1 y) + \delta_2 \cosh(\lambda_2 y), \tag{2.22c}$$

with

$$\phi_1 = \frac{1}{a_3 - a_1}\left[a_2\theta_1 - \frac{a_3}{a_6}\lambda_1\gamma_1\right], \quad \phi_2 = \frac{1}{a_3 - a_1}\left[a_2\theta_2 - \frac{a_3}{a_6}\lambda_2\gamma_2\right], \tag{2.23a,b}$$

$$\theta_1 = -\frac{\gamma_1 a_4}{\lambda_1 a_5}, \quad \theta_2 = -\frac{\gamma_2 a_4}{\lambda_2 a_5}, \tag{2.23c,d}$$

$$\delta_1 = \frac{1}{a_3 - a_1}\left[\frac{a_1}{a_6}\lambda_1\gamma_1 - a_2\theta_1\right], \quad \delta_2 = \frac{1}{a_3 - a_1}\left[\frac{a_1}{a_6}\lambda_2\gamma_2 - a_2\theta_2\right]. \tag{2.23e,f}$$

Notice that, upon substituting into (2.13$d$), we find that the constant arising from the integration of (2.13$b$) must vanish.

### 2.3. *Results*

Figure 4 shows a typical equilibrium bed configuration predicted by the two-dimensional theory. It appears that a strong longitudinal deformation characterizes the bottom profile, with deposition occurring at the wide section and scour at the channel narrowing. The bed profile $\eta_1$ ($= H_1 - D_1$) is nearly in phase with the banks, as shown in figure 5, in agreement with the experimental observations presented in § 4. A similar behaviour has been also observed by Bittner (1994). In this respect the present findings do not differ significantly from results which could be obtained through a simpler one-dimensional model. A longitudinal perturbation of cross-sectionally-averaged velocity is associated with bed topography, which attains its maximum positive value almost exactly at the narrowest section (figure 5).

It is worth noting that the two-dimensional solution exhibits a right qualitative overall pattern. However, the model does not predict any significant transverse bed deformation as shown in figure 4. Hence, predicted transverse variations of the flow field are very weak with respect to longitudinal variations. In light of the speculations put forward in § 1, we can readily argue that the two-dimensional model always

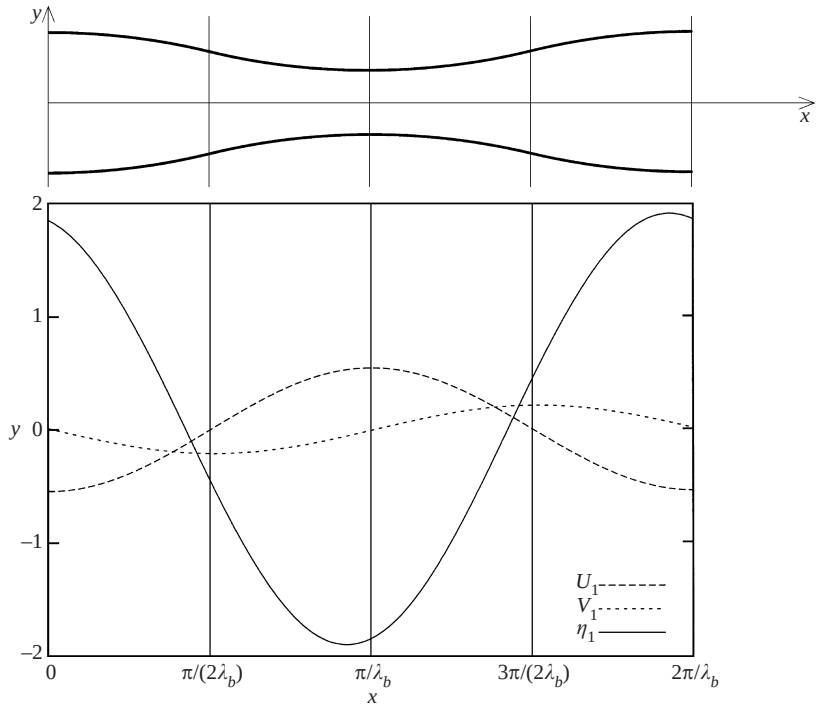


FIGURE 5. Two-dimensional model. Longitudinal profiles of depth-averaged velocity components $(U_1, V_1)$ and bed elevation $\eta_1$ at the bank: $\lambda_b = 0.2$, $\beta = 15$, $\vartheta_0 = 0.07$, $d_s = 0.05$.

predicts stability of the planform since the stress distribution matches the one shown in figure 3(*b*). Hence, within the context of a depth-averaged model, width variations which are induced by the recursive formation of alternating bars in single channels of braided networks, as observed by Ashmore (1982, 1991), do not seem to provide a suitable mechanism able to promote channel bifurcation. To overcome this difficulty we introduce a three-dimensional approach in the next section; furthermore, in § 6 we will show how the predictions of the two-dimensional model can be improved when the effect of streamline curvature on the transverse bed shear stress is taken into account.

Also notice that, like the analogous problem of a periodic variation of channel curvature, the present solution displays a resonant behaviour under suitable conditions. Resonance occurs when the forcing effect of the variable planform is such as to excite a steady free response of the channel with the same planimetrical structure as the forced pattern. In the case of meandering channels Blondeaux & Seminara (1985) showed how alternate bars could be resonantly excited by channel curvature. In our case the situation is similar; however, the forcing effect is symmetrical with respect to channel axis and it can only excite symmetrical free forms such as central bars (or even higher-order transverse modes). An example of resonant behaviour is given in figure 6 where the difference between bed elevation at the centreline and at the banks is plotted versus the wavenumber of width variations. It appears that, close to resonant conditions, the transverse deformation of the bed profile is strongly enhanced and its amplitude tends to infinity when the resonant condition is exactly met. Of course, under this condition the linear theory becomes invalid; a weakly nonlinear approach can be introduced, like that proposed by Seminara & Tubino

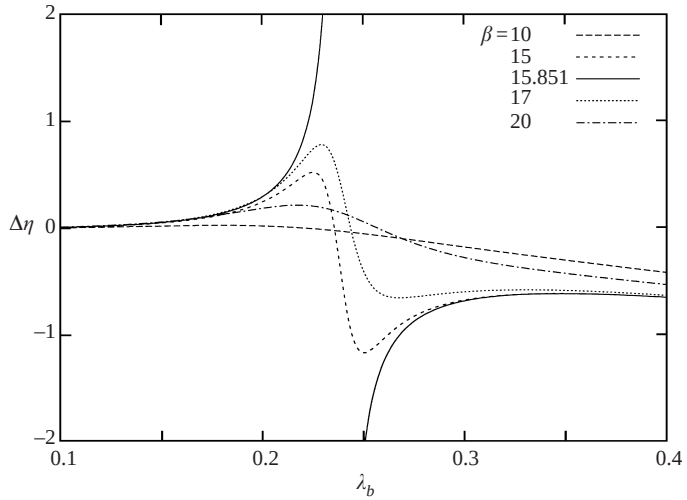


FIGURE 6. Two-dimensional model. The difference $\Delta\eta = \eta_1(0) - \eta_1(1)$ between bed elevation at the centreline and at the bank (at the widest section) is plotted versus the wavenumber of width variations $\lambda_b$, for different values of the aspect ratio $\beta$: $\vartheta_0 = 0.07$, $d_s = 0.05$; $\beta = 15.851$ corresponds to the resonant value.

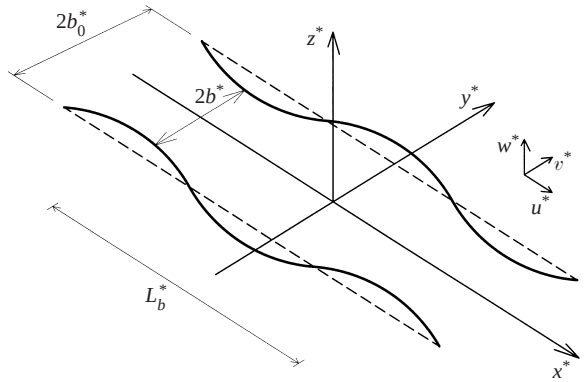


FIGURE 7. Sketch of channel geometry and notation.

(1992) to investigate resonant meanders. It is interesting to note that, unlike in the case of meandering channels, here the range of parameters in which resonance affects the results seems to be quite narrow.

## 3. Three-dimensional model

### 3.1. *Formulation of the problem*

In this section, we develop a three-dimensional model to determine the flow and bed structure of a cohesionless straight channel subject to periodic width variations. Referring to figure 7, let $x^*$, $y^*$ and $z^*$ be the longitudinal, transverse and normal to the average bed coordinates, respectively. Furthermore, let $u^*$, $v^*$ and $w^*$ be the corresponding velocity components. The equation describing channel banks is given by (2.1*a*).

As shown in § 2 we work in a stretched domain in which the transverse coordinate is normalized with the local width, according to equation (2.2). Further dimensionless

variables are defined as follows

$$\boldsymbol{u}^* = (u^*, v^*, w^*) = U_0^* \left(u, v, \frac{w}{\beta}\right), \quad z^* = D_0^* z, \quad v_t^* = \sqrt{C_{f0}} U_0^* D_0^* v_t, \tag{3.1a–c}$$

where $v_t$ is the kinematic eddy viscosity. According to the shallow-water approximation, the dimensionless Reynolds equations under steady conditions have the form:

$$uu_{,x} + (uN_1 + vN_0)u_{,y} + wu_{,z} - \beta\sqrt{C_{f0}}(v_t u_{,z})_{,z} + F_0^{-2}H_{,x} + F_0^{-2}N_1 H_{,y} = 0, \tag{3.2a}$$

$$uv_{,x} + (uN_1 + vN_0)v_{,y} + wv_{,z} - \beta\sqrt{C_{f0}}(v_t v_{,z})_{,z} + F_0^{-2}N_0 H_{,y} = 0, \tag{3.2b}$$

$$u_{,x} + N_1 u_{,y} + N_0 v_{,y} + w_{,z} = 0, \tag{3.2c}$$

where $N_0(x)$ and $N_1(x, y)$ arise from the transformation (2.2) and are

$$N_0(x) = [1 + \delta(\exp(\mathrm{i}\lambda_b x) + \text{c.c.})]^{-1}, \tag{3.3a}$$

$$N_1(x, y) = -y\lambda_b\delta(\mathrm{i}\exp(\mathrm{i}\lambda_b x) + \text{c.c.})N_0. \tag{3.3b}$$

The boundary conditions for equations (3.2*a–c*) read

$$u = v = w = 0 \quad (z = \eta + z_0 D), \tag{3.4a}$$

$$\beta w - (N_0 v + N_1 u)H_{,y} - uH_{,x} = 0 \quad (z = H), \tag{3.4b}$$

$$u_{,z} = v_{,z} = 0 \quad (z = H), \tag{3.4c}$$

$$\int_D \boldsymbol{u} \cdot \hat{\boldsymbol{n}}_b \mathrm{d}z = 0 \quad (y = \pm 1), \tag{3.4d}$$

where $\eta = (H - D)$ is the local bed elevation and $\hat{\boldsymbol{n}}_b$ is the unit vector normal to the banks. They express the no-slip condition at the bed (with $z_0$ the reference level at which the condition is imposed under uniform conditions), the kinematic and dynamic conditions at the free surface (in the simplified form which follows from the shallow-water approximation) and the kinematic condition at the banks.

Flow equations are then coupled with the sediment continuity (2.4*d*) with the associated boundary conditions (2.6*b*).

A slowly varying approach is adopted to introduce the closure relationships required to complete the formulation of the problem. Hence, we define

$$v_t = \sqrt{\frac{C_f}{C_{f0}}}|\boldsymbol{U}|D\mathcal{N}(\zeta), \tag{3.5}$$

where the vertical structure of the turbulent kinematic viscosity is given in terms of the stretched vertical variable $\zeta$ according to the relationship proposed by Dean (1974)

$$\mathcal{N}(\zeta) = \frac{k\zeta}{1 + \zeta + 4.68\zeta^2}, \quad \zeta = \frac{z - \eta}{D}, \tag{3.6a, b}$$

where $k$ is the von Kármán constant. Furthermore, the friction factor is evaluated through equation (2.8*a*).

Bed load transport is treated as described in § 2.

### 3.2. *Linearization*

We take advantage of the assumption of small amplitude of width variations ($\delta \ll 1$) and expand the solution in the form

$$(u, v, w, H, D) = (u_0, 0, 0, \bar{H}, 1) + \delta[(u', v', w', h, d)\exp(\mathrm{i}\lambda_b x) + \text{c.c.}] + O(\delta^2), \tag{3.7}$$

where $u_0(\zeta)$ is the velocity profile of the basic uniform flow in the straight channel with constant width $2b_0^*$. Substituting the expansion (3.7) into equations (3.2*a–c*) and (3.4*a–d*) and keeping only linear terms, the following differential problem for the variables $u'$, $v'$, $w'$, $h$ and $d$ is obtained:

$$(\mathcal{N} v'_{,\zeta})_{,\zeta} - \frac{\mathrm{i}\lambda_b u_0 v'}{\beta\sqrt{C_{f0}}} - \frac{h_{,y}}{\beta F_0^2\sqrt{C_{f0}}} = 0, \tag{3.8a}$$

$$(\mathcal{N} u'_{,\zeta})_{,\zeta} - \frac{\mathrm{i}\lambda_b u_0 u'}{\beta\sqrt{C_{f0}}} - \sqrt{C_{f0}}\left(\tfrac{1}{2}C_D d + \int_{z_0}^{1} u'\,\mathrm{d}\zeta\right) - \frac{w'}{\beta\sqrt{C_{f0}}}\frac{\mathrm{d}u_0}{\mathrm{d}\zeta} + \frac{\mathrm{i}\lambda_b u_0}{\beta\sqrt{C_{f0}}}\frac{\mathrm{d}u_0}{\mathrm{d}\zeta}[h - d(1-\zeta)] - \frac{\mathrm{i}\lambda_b h}{\beta F_0^2\sqrt{C_{f0}}} + \sqrt{C_{f0}}d = 0, \tag{3.8b}$$

$$w'_{,\zeta} + \mathrm{i}\lambda_b u' - \mathrm{i}\lambda_b \frac{\mathrm{d}u_0}{\mathrm{d}\zeta}[h - d(1-\zeta)] + v'_{,y} = 0, \tag{3.8c}$$

with the boundary conditions

$$w' - \mathrm{i}\lambda_b h u_0 = 0, \quad v'_{,\zeta} = u'_{,\zeta} = 0 \quad (\zeta = 1), \tag{3.9a–c}$$

$$u' = v' = w' = 0 \qquad (\zeta = z_0), \tag{3.10a–c}$$

$$\int_{z_0}^{1} v'\,\mathrm{d}\zeta = \pm\mathrm{i}\lambda_b \qquad (y = \pm 1). \tag{3.11a, b}$$

The linearized form of the sediment continuity equation (2.4*d*) is

$$\mathrm{i}\lambda_b \Phi_T\left[\tfrac{1}{2}C_D d + \int_{z_0}^{1} u'\,\mathrm{d}\zeta + \frac{(\mathcal{N}u'_{,\zeta})_{z_0}}{\sqrt{C_{f0}}}\right] + \left(\frac{v'_{,\zeta y}}{\mathrm{d}u_0/\mathrm{d}\zeta}\right)_{z_0} - \frac{r}{\beta\sqrt{\vartheta_0}}(h-d)_{,yy} = 0, \tag{3.12}$$

with the boundary conditions

$$\left(\frac{v'_{,\zeta}}{\mathrm{d}u_0/\mathrm{d}\zeta}\right)_{z_0} - \frac{r}{\beta\sqrt{\vartheta_0}}(h-d)_{,y} = \pm\mathrm{i}\lambda_b \quad (y = \pm 1). \tag{3.13a, b}$$

### 3.3. *Solution*

We first integrate the continuity equation (3.8*c*) to find an explicit expression for the vertical velocity component $w'$ as follows:

$$w' = -\mathscr{G}_{,y} - \mathrm{i}\lambda_b \mathscr{F} + \mathrm{i}\lambda_b d\left[u_0(\zeta - 1) - \int_{z_0}^{\zeta} u_0\,\mathrm{d}\zeta\right] + \mathrm{i}\lambda_b u_0 h, \tag{3.14}$$

where

$$\mathscr{F} = \int_{z_0}^{\zeta} u'\,\mathrm{d}\zeta, \quad \mathscr{G} = \int_{z_0}^{\zeta} v'\,\mathrm{d}\zeta. \tag{3.15a, b}$$

From equations (3.8*a, b*), substituting (3.14) into (3.8*b*), we find the following differ-

ential problem

$$\mathscr{G}_{,\zeta\zeta\zeta} = -\frac{1}{\mathscr{N}}\frac{\mathrm{d}\mathscr{N}}{\mathrm{d}\zeta}\mathscr{G}_{,\zeta\zeta} + \frac{\mathrm{i}\lambda_b u_0}{\beta\sqrt{C_{f0}}\mathscr{N}}\mathscr{G}_{,\zeta} + \frac{h_{,y}}{\beta F_0^2\sqrt{C_{f0}}\mathscr{N}}, \tag{3.16a}$$

$$\mathscr{F}_{,\zeta\zeta\zeta} = -\frac{1}{\mathscr{N}}\frac{\mathrm{d}\mathscr{N}}{\mathrm{d}\zeta}\mathscr{F}_{,\zeta\zeta} + \frac{\mathrm{i}\lambda_b u_0}{\beta\sqrt{C_{f0}}\mathscr{N}}\mathscr{F}_{,\zeta} - \frac{\mathrm{i}\lambda_b}{\beta\sqrt{C_{f0}}\mathscr{N}}\frac{\mathrm{d}u_0}{\mathrm{d}\zeta}\mathscr{F} - \frac{1}{\beta\sqrt{C_{f0}}\mathscr{N}}\frac{\mathrm{d}u_0}{\mathrm{d}\zeta}\mathscr{G}_{,y} +$$
$$-\frac{\mathrm{i}\lambda_b d}{\beta\sqrt{C_{f0}}\mathscr{N}}\frac{\mathrm{d}u_0}{\mathrm{d}\zeta}\int_{z_0}^{\zeta} u_0\mathrm{d}\zeta + \frac{\mathrm{i}\lambda_b h}{\beta F_0^2\sqrt{C_{f0}}\mathscr{N}} + \frac{\sqrt{C_{f0}}}{\mathscr{N}}\left[\left(\tfrac{1}{2}C_D - 1\right)d + \mathscr{F}(1)\right], \tag{3.16b}$$

with the boundary conditions

$$\mathscr{G}_{,\zeta\zeta} = \mathscr{F}_{,\zeta\zeta} = 0 \quad (\zeta = 1), \tag{3.17a, b}$$

$$\mathscr{G}_{,\zeta} = \mathscr{G} = \mathscr{F}_{,\zeta} = \mathscr{F} = 0 \quad (\zeta = z_0), \tag{3.18a–d}$$

$$\mathscr{G} = \pm\mathrm{i}\lambda_b \quad (\zeta = 1, y = \pm 1), \tag{3.19a, b}$$

$$\left(\frac{\mathscr{G}_{,\zeta\zeta}}{\mathrm{d}u_0/\mathrm{d}\zeta}\right)_{z_0} - \frac{r}{\beta\sqrt{\vartheta_0}}(h-d)_{,y} = \pm\mathrm{i}\lambda \quad (y = \pm 1). \tag{3.20a, b}$$

Boundary conditions (3.19*a*, *b*) and (3.20*a*, *b*) suggest the following structure for the solution:

$$\mathscr{G} = \mathscr{G}_0(\zeta)y + \sum_{m=1}^{\infty}\mathscr{G}_m(\zeta)\sin(m\pi y), \tag{3.21a}$$

$$(\mathscr{F}, h, d) = [\hat{\mathscr{F}}(\zeta), \hat{h}, \hat{d}]y^2 + \sum_{m=0}^{\infty}[\mathscr{F}_m(\zeta), h_m, d_m]\cos(m\pi y). \tag{3.21b}$$

Substituting from (3.21*a*, *b*) into (3.16*a*, *b*) leads to a sequence of ordinary differential boundary-value problems in the variable $\zeta$, which are solved numerically using a 'shooting' procedure along with a fourth-order Runge–Kutta scheme.

The solution procedure is reported in detail in Appendix A.

### 3.4. *Results*

Figures 8(*a*)–8(*d*) show the results for bottom configuration ($\eta' = h - d$) induced by width variations, for increasing values of the wavenumber $\lambda_b$; the corresponding amplitudes of the leading components of the Fourier representation of the bed profile are reported in figures 9(*a*)–9(*d*). The first contribution (denoted by 0) represents a purely longitudinal bottom deformation, which corresponds to deposition at the wide section and scour at the narrow section. This is where the cross-sectionally averaged velocity attains its maximum value. The 0-component is nearly in phase with respect to the bank profile, in agreement with theoretical findings based on the two-dimensional model (§ 2) and experimental observations described in the next section. The novel feature associated with the three-dimensional model is the appearance of a second leading contribution (denoted by 1) which implies a transverse deformation of the bed, with transverse wavelength equal to channel width. Its amplitude changes with $\lambda_b$ and reaches a maximum for $\lambda_b$ ranging about 0.3 (figure 9*a–d*), which corresponds to a longitudinal wavelength of about 10 channel widths. Under these conditions, the amplitude of the latter harmonic is comparable with that of harmonic 0, both

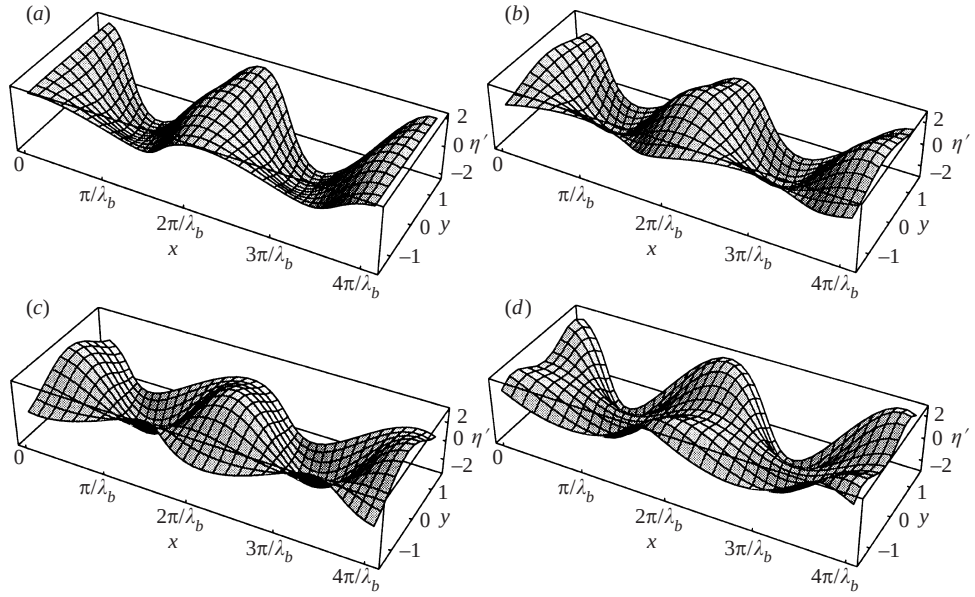


FIGURE 8. Three-dimensional model. Equilibrium bed configurations for different values of the wavenumber of width variations: $\vartheta_0 = 0.1$, $d_s = 0.05$, $\beta = 15$. (*a*) $\lambda_b = 0.1$, (*b*) 0.2, (*c*) 0.3, (*d*) 0.5.

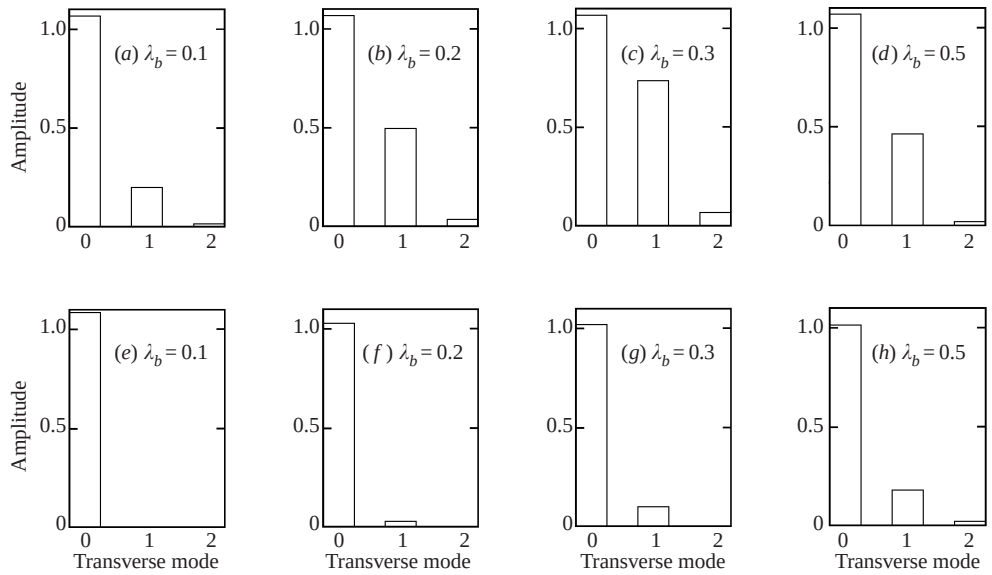


FIGURE 9. Amplitude of the leading transverse modes (with longitudinal wavenumber equal to $\lambda_b$) of the Fourier representation of bed elevation obtained with (*a–d*) the three-dimensional model, and (*e–h*) the two-dimensional model, for different values of $\lambda_b$: $\vartheta_0 = 0.1$, $d_s = 0.05$, $\beta = 15$.

for the bed elevation and for the longitudinal velocity. The relative position of the transverse component with respect to bank profile changes significantly with the wavelength of width variations as shown in figure 8(*a–d*); as $\lambda_b$ increases, its peak moves downstream: while at $\lambda_b = 0.1$ the 1-component lags behind the 0-component, when $\lambda_b = 0.5$ the phase shift becomes so large that the two main components of

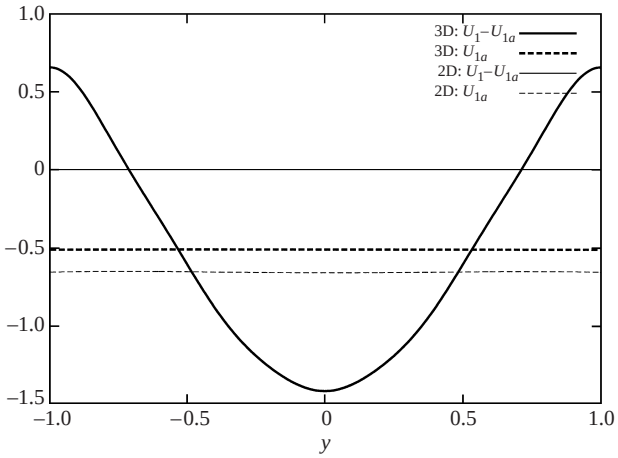


FIGURE 10. Difference between the longitudinal depth-averaged velocity $U_1$ and the longitudinal cross-sectionally averaged velocity $U_{1a}$ at the widest section (2D, two-dimensional model; 3D, three-dimensional model): $\beta = 20$, $\lambda_b = 0.2$, $\vartheta_0 = 0.1$, $d_s = 0.05$.

the bed profile are nearly out of phase, leading to the bottom configuration plotted in figure 8(*d*). It is worth noting that the 1-component displays the spatial structure of central bars, with longitudinal wavelength equal to that of width variations. As illustrated in figure 9(*a–d*), higher-order transverse modes (denoted by 2, ...) are found to be small for all values of $\lambda_b$.

From the comparison between three- and two-dimensional findings reported in figure 9(*a–h*), it appears that the transverse deformation of the bed is mainly related to three-dimensional effects since the 1-component is nearly absent in the resulting topography of the two-dimensional model. Notice that the transverse deformation of the bed associated with the 1-component also implies a transverse distortion of the primary (longitudinal) flow, as illustrated in figure 10 where the results of the two-dimensional model are also included. It appears that the above effect may counteract, at the banks, the overall reduction of longitudinal velocity which occurs in the widest section, leading to positive values of the perturbation of longitudinal velocity. The corresponding distribution of bank stress matches the 'unstable' distribution depicted in figure 3(*c*). As a result the generation of a central bar pattern pushes the thread of high velocity toward the banks, leading to flow divergence in the widest part of the channel. This mechanism is inherently associated with secondary flows which are driven by centrifugal effects induced by streamline curvature and convective acceleration which are accounted for in the three-dimensional model. The effect of the secondary flow on the central bar is analogous to the effect of secondary flow on curvature-forced bars (point bars) in meandering rivers. In that sense the central bar can be thought of as a pair of coupled back-to-back point bars (Bridge & Gabel 1992). The role of streamline curvature in producing secondary flow is further discussed in § 6. Circulation in the $(y, z)$-plane is also triggered by the convective term appearing in equation (3.8*aa*), which vanishes at the bed and reaches its maximum at the free surface. This implies a phase shift in the response of transverse velocity to the variable width, as shown in figure 11(*a*). Just downstream of the narrowest section the transverse velocity near the bottom is directed outward while streamlines are still converging at the free surface. The resulting circulation, sketched in figure 11(*b*), induces a transverse deformation of the bed (figure 11*c*) which in turn affects the

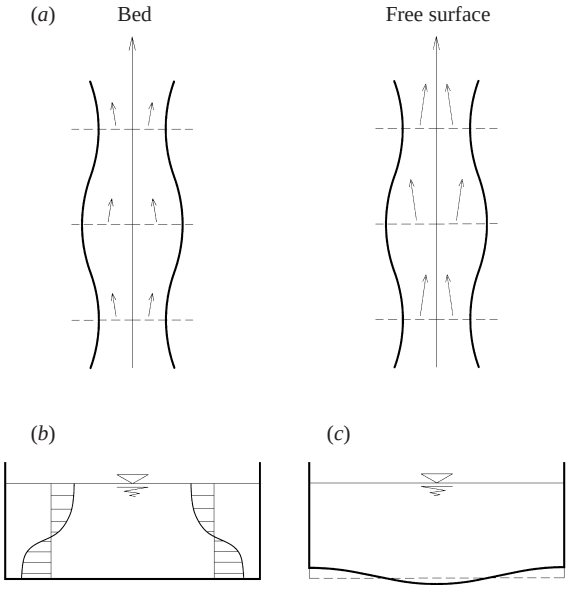


FIGURE 11. (*a*) Mechanism of generation of secondary flow due to transverse flow adjustment to spatial variations of bank profile. (*b*) Sketch of secondary flow and (*c*) of the resulting bed deformation at the narrowest section.

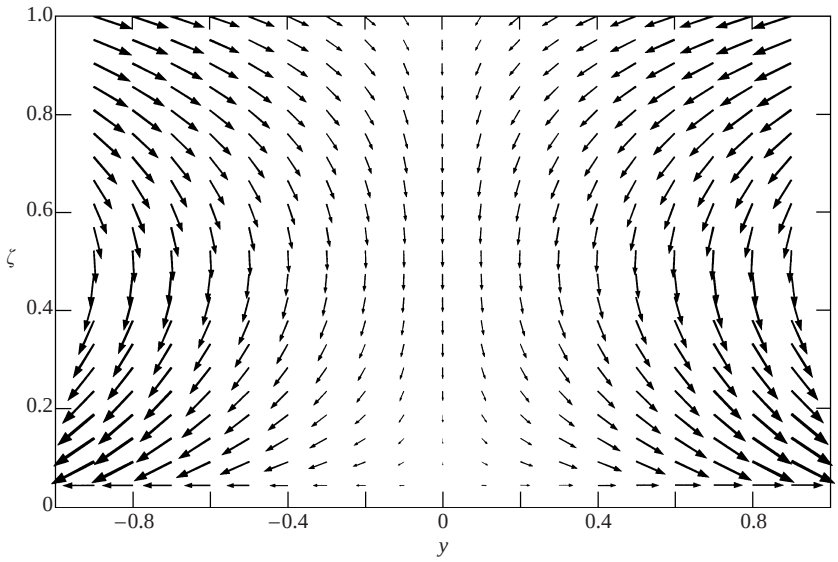


FIGURE 12. Secondary flow in the $(y,\zeta)$-plane at the narrowest section: $\beta = 15$, $\lambda_b = 0.2$, $\vartheta_0 = 0.1$, $d_s = 0.05$. The local depth-averaged value has been filtered out from the transverse velocity component.

transverse distribution of longitudinal velocity. A similar mechanism operates in the widest section and promotes the formation of a central bar.

In figure 12 the velocity field in the $(y,\zeta)$-plane at the narrowest section is plotted, showing a secondary circulation.

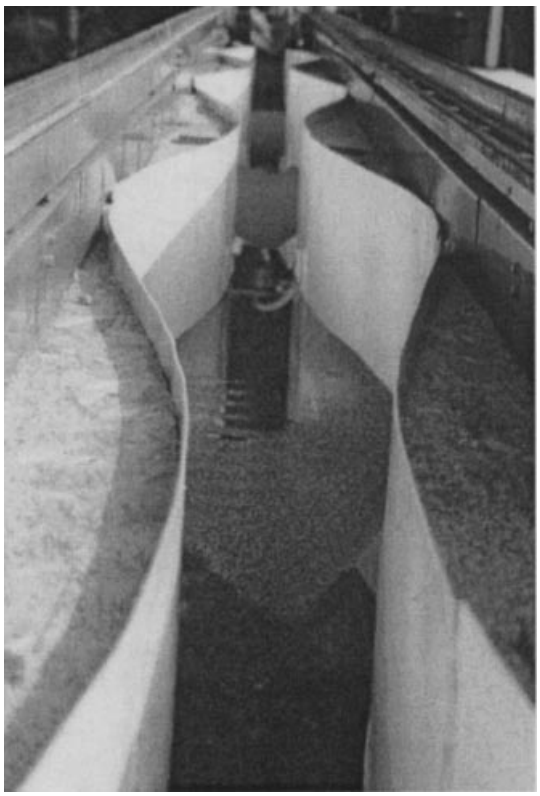

FIGURE 13. The experimental flume (Hydraulic Laboratory, Trento University, Italy).

## 4. Experimental study

We carried out experiments in a flume with a length of 15 m and a maximum width of 60 cm (figure 13) in the Hydraulic Laboratory of Trento University. Periodic width variations were constructed inside the channel by attaching strips of PVC to wooden profiles, to form vertical flume walls; the bank configuration considered is described by equation (2.1). Three different bank configurations have been tested and their geometrical characteristics ($\lambda_b$ and $\delta$) are summarized in tables 1, 2 and 3.

The flume was filled with a well-sorted 1.36 mm sediment, recirculated through a cyclone pump from the channel downstream end to a second hydrocyclone, installed at the head of the flume, where the sediment and the water used to recirculate it were separated. Water level inside the tank was set using a sluice gate. Bed elevation was surveyed, in the absence of water flow, using a laser profiler mounted on a carriage driven by a motor along longitudinal and transverse directions.

The experiments involved different water discharges and slopes, which correspond to the following ranges of values of dimensionless parameters: $5.5 < \beta < 18$, $\vartheta_c < \vartheta_0 < 0.13$, $0.05 < d_s < 0.12$. Experimental conditions are summarized in tables 1, 2 and 3 where $S$ is the average slope, $Q$ is flow discharge, $D_0^*$ is the average flow depth and $2b_0^*$ is the average width.

During each experiment water discharge and water level were periodically measured along the flume and sediment discharge was collected using a trap placed at the downstream end of the channel. The shape and position of bedforms in the channel were periodically sketched and the migration speed of bars was estimated. Once

| Run | $S$ | $Q\,(s^{-1})$ | $D_0^*\,(m)$ | $\beta$ | $\vartheta_0$ | $d_s$ |
|---|---|---|---|---|---|---|
| 1† | 0.007 | 1.87 | 0.015 | 13.46 | 0.046 | 0.091 |
| 2† | 0.007 | 4.96 | 0.026 | 7.70 | 0.081 | 0.052 |
| 3 | 0.007 | 4.96 | 0.026 | 7.70 | 0.081 | 0.052 |
| 4 | 0.007 | 5.32 | 0.027 | 7.43 | 0.084 | 0.050 |
| 5 | 0.007 | 5.43 | 0.028 | 7.18 | 0.087 | 0.049 |
| 6 | 0.007 | 5.88 | 0.029 | 6.94 | 0.090 | 0.047 |
| 7 | 0.007 | 3.66 | 0.022 | 9.19 | 0.068 | 0.062 |
| 8 | 0.007 | 3.66 | 0.022 | 9.19 | 0.068 | 0.062 |
| 9 | 0.007 | 3.99 | 0.023 | 8.75 | 0.071 | 0.059 |
| 10‡ | 0.007 | 2.81 | 0.019 | 10.61 | 0.059 | 0.072 |
| 11† | 0.007 | 2.93 | 0.019 | 10.27 | 0.061 | 0.070 |
| 12 | 0.007 | 4.96 | 0.026 | 7.70 | 0.081 | 0.052 |
| 13‡ | 0.010 | 1.81 | 0.013 | 14.97 | 0.059 | 0.102 |
| 14† | 0.010 | 1.36 | 0.011 | 17.68 | 0.050 | 0.120 |
| 15 | 0.010 | 3.28 | 0.019 | 10.77 | 0.083 | 0.073 |
| 16 | 0.010 | 3.63 | 0.020 | 10.21 | 0.087 | 0.069 |
| 17 | 0.010 | 2.32 | 0.015 | 13.14 | 0.068 | 0.089 |
| 18 | 0.010 | 3.28 | 0.019 | 10.77 | 0.083 | 0.073 |
| 19‡ | 0.010 | 1.36 | 0.011 | 17.68 | 0.050 | 0.120 |
| 20† | 0.015 | 1.64 | 0.011 | 17.77 | 0.075 | 0.121 |
| 21 | 0.015 | 1.64 | 0.011 | 17.77 | 0.075 | 0.121 |
| 22 | 0.015 | 2.38 | 0.014 | 14.35 | 0.093 | 0.098 |

† Experiments in which bed topography was not surveyed in detail;
‡ Experiments whose results are not reported in figures 14, 15, 16 and 17 since they were characterized by values of the Shields parameter close to the threshold value for incipient motion.

TABLE 1. Geometrical characteristics of the experimental channel and flow and sediment transport parameters: $\lambda_b = 0.5$; $\delta = 0.125$; $2b_0^* = 0.40\,m$.

the bottom had reached a quasi-steady condition, the pumps were switched off, the downstream sluice gate was closed and a backwater profile was generated to prevent the dissection of bed topography; the flume was then slowly emptied. When the bed surface was dry, bottom elevation was surveyed using the laser profiler, measuring 50 points in each cross-section with a longitudinal spacing of 10 cm. Furthermore, the position and length of each bar in the flume were measured in detail. Finally, bottom elevation data were analysed through a fast Fourier transform procedure.

Experimental observations show that the variable planform induces an altimetrical bed response which significantly differs from that found in constant width channels.

For small-amplitude width variations ($\delta = 0.125$) and sufficiently large width/depth ratio, migrating alternate bars formed in the flume. This behaviour is in general agreement with theoretical predictions of Colombini, Seminara & Tubino (1987). However, the development of the migrating bars was strongly obstructed by the variable bank configuration; the development of alternate bars was always irregular and highly unsteady. The beginning of each experiment was usually characterized by the formation of central bars at the wide sections of the flume. Such bars, once they reached a sufficient amplitude, started to migrate downstream with a speed ranging between $5\,cm\,min^{-1}$ and $15\,cm\,min^{-1}$, depending on the hydraulic conditions of the experiment. The migration speed decreased significantly as the front of the bar approached the narrowest section of the flume. Usually the central bar could not migrate through the constraint; hence, a temporary configuration was

| Run | $S$ | $Q\,(s^{-1})$ | $D_0^*\,(m)$ | $\beta$ | $\vartheta_0$ | $d_s$ |
|---|---|---|---|---|---|---|
| 23 | 0.015 | 2.43 | 0.014 | 14.29 | 0.094 | 0.097 |
| 24 | 0.015 | 3.19 | 0.016 | 12.20 | 0.110 | 0.083 |
| 25 | 0.015 | 2.88 | 0.015 | 12.93 | 0.103 | 0.088 |
| 26 | 0.015 | 1.64 | 0.011 | 17.77 | 0.075 | 0.121 |
| 27† | 0.015 | 3.81 | 0.018 | 11.01 | 0.121 | 0.075 |
| 28† | 0.015 | 1.94 | 0.012 | 16.16 | 0.083 | 0.110 |
| 29 | 0.015 | 3.81 | 0.018 | 11.01 | 0.121 | 0.075 |
| 30 | 0.015 | 3.33 | 0.017 | 11.88 | 0.112 | 0.081 |
| 31 | 0.015 | 2.43 | 0.014 | 14.29 | 0.094 | 0.097 |
| 32 | 0.015 | 3.33 | 0.017 | 11.88 | 0.112 | 0.081 |
| 33† | 0.015 | 3.81 | 0.018 | 11.01 | 0.121 | 0.075 |
| 34 | 0.015 | 1.64 | 0.011 | 17.77 | 0.080 | 0.121 |
| 35‡ | 0.010 | 1.67 | 0.013 | 15.75 | 0.057 | 0.107 |
| 36 | 0.010 | 2.90 | 0.017 | 11.45 | 0.078 | 0.078 |
| 37 | 0.010 | 2.45 | 0.016 | 12.65 | 0.070 | 0.086 |
| 38 | 0.010 | 3.28 | 0.019 | 10.77 | 0.083 | 0.073 |
| 39 | 0.010 | 3.91 | 0.021 | 9.74 | 0.091 | 0.066 |
| 40 | 0.010 | 1.99 | 0.014 | 14.29 | 0.062 | 0.097 |
| 41 | 0.010 | 4.89 | 0.023 | 8.57 | 0.104 | 0.058 |
| 42 | 0.010 | 2.32 | 0.015 | 13.14 | 0.068 | 0.089 |
| 43 | 0.010 | 3.63 | 0.020 | 10.21 | 0.087 | 0.069 |
| 44‡ | 0.010 | 1.36 | 0.011 | 17.68 | 0.050 | 0.120 |
| 45‡ | 0.007 | 2.50 | 0.018 | 11.37 | 0.055 | 0.077 |
| 46 | 0.007 | 3.25 | 0.021 | 9.68 | 0.064 | 0.066 |
| 47 | 0.007 | 4.96 | 0.026 | 7.70 | 0.081 | 0.052 |
| 48 | 0.007 | 5.88 | 0.029 | 6.94 | 0.090 | 0.047 |
| 49 | 0.007 | 2.93 | 0.019 | 10.27 | 0.061 | 0.070 |
| 50 | 0.007 | 4.66 | 0.025 | 8.02 | 0.078 | 0.054 |
| 51 | 0.007 | 5.31 | 0.027 | 7.42 | 0.084 | 0.050 |
| 52 | 0.007 | 5.12 | 0.027 | 7.55 | 0.083 | 0.051 |
| 53 | 0.007 | 4.86 | 0.026 | 7.96 | 0.079 | 0.053 |
| 54 | 0.007 | 4.75 | 0.026 | 7.78 | 0.080 | 0.053 |
| 55† | 0.004 | 4.60 | 0.030 | 6.77 | 0.053 | 0.046 |
| 56† | 0.004 | 4.98 | 0.031 | 6.50 | 0.055 | 0.044 |
| 57† | 0.004 | 5.11 | 0.032 | 6.26 | 0.057 | 0.043 |
| 58† | 0.004 | 5.82 | 0.034 | 5.86 | 0.061 | 0.040 |
| 59† | 0.004 | 6.77 | 0.037 | 5.52 | 0.065 | 0.037 |

† Experiments in which bed topography was not surveyed in detail;
‡ Experiments whose results are not reported in figures 14, 15, 16 and 17 since they were characterized by values of the Shields parameter close to the threshold value for incipient motion.

TABLE 2. Geometrical characteristics of the experimental channel and flow and sediment transport parameters: $\lambda_b = 0.3$; $\delta = 0.125$; $2b_0^* = 0.40\,m$.

established in which sediment transport occurred mainly at the channel sides within the narrowest sections and at the centreline within the widest sections. Individual bars were swallowed up in the downstream narrows and new bars formed in the upstream expansion. As a response the central bar pattern decayed into a series of short alternate bars, with a migration speed varying from a few $cm\,min^{-1}$ to a maximum of $20\,cm\,min^{-1}$. Regular trains of bars migrating along the full length of the channel never developed; rather, the characteristic process was pulsating, with repeated formation and obliteration of bars with variable length and height.

| Run | $S$ | $Q\,(\mathrm{s}^{-1})$ | $D_0^*\,(\mathrm{m})$ | $\beta$ | $\vartheta_0$ | $d_s$ |
|---|---|---|---|---|---|---|
| 60‡ | 0.004 | 4.13 | 0.028 | 7.22 | 0.049 | 0.049 |
| 61‡ | 0.004 | 4.98 | 0.031 | 6.50 | 0.055 | 0.044 |
| 62† | 0.004 | 3.25 | 0.024 | 8.17 | 0.044 | 0.056 |
| 63 | 0.007 | 3.25 | 0.021 | 9.68 | 0.064 | 0.066 |
| 64‡ | 0.007 | 2.50 | 0.018 | 11.37 | 0.055 | 0.077 |
| 65‡ | 0.007 | 2.50 | 0.018 | 11.37 | 0.055 | 0.077 |
| 66 | 0.007 | 3.99 | 0.023 | 8.75 | 0.071 | 0.059 |
| 67 | 0.007 | 5.88 | 0.029 | 6.94 | 0.090 | 0.047 |

† Experiments in which bed topography was not surveyed in detail;
‡ Experiments whose results are not reported in figures 14, 15, 16 and 17 since they were characterized by values of the Shields parameter close to the threshold value for incipient motion.

TABLE 3. Geometrical characteristics of the experimental channel and flow and sediment transport parameters: $\lambda_b = 0.3$; $\delta = 0.25$; $2b_0^* = 0.40\,\mathrm{m}$.

At $\delta = 0.25$ alternate bars were suppressed in favour of a steady forced bed configuration.

For all geometric configurations, the final topography displayed a strong steady longitudinal deformation, almost in phase with the bank profile, whose amplitude increased with the Shields parameter. A transverse deformation, in the shape of a central bar deposited in the wide section, was also found, with amplitude of the same order of magnitude as the longitudinal one.

These results suggest that periodic width variations may trigger the transition from migrating alternate bars to a steady symmetrical bed configuration (steady central bars) with dominant longitudinal wavenumber equal to that of the bank profile.

## 5. Comparison of experimental and theoretical findings

In this section theoretical results are compared with experimental findings. Figure 14 shows that an overall agreement is found between theoretical predictions of the difference $\Delta A$ between the maximum and minimum bed elevation within a wavelength and experimental values. A detailed comparison is given in figures 15$(a,b)$, 16$(a,b)$ and 17$(a,b)$ in terms of the amplitude of the leading components of the Fourier representation of bed topography. We denote with '0' the harmonic corresponding to a purely longitudinal deformation, with longitudinal wavelength equal to that of width variations, and with '1' the harmonic corresponding to central bars.

The agreement is satisfactory for the transverse mode '0' in all cases (figure 15$a$). For $\delta = 0.25$ the theory underestimates slightly the values of longitudinal bed deformation. Notice, however, that in this case the amplitude of width variations is relatively large; hence a linearized theory may not be completely adequate to describe the solution. Both theoretical and experimental results for the harmonic '0' do not display a significant dependence on the average Shields stress $\vartheta_0$; some examples are reported in figures 16$(a)$ and 17$(a)$ where each plot corresponds to a different initial bed slope.

As for the amplitude of the central bar mode '1', the comparison with experimental findings must be considered with more care. Figure 17$(b)$ shows that, for suitable values of the controlling dimensionless parameters, the theory displays a resonant response which implies that the amplitude of the harmonic '1' tends to infinity

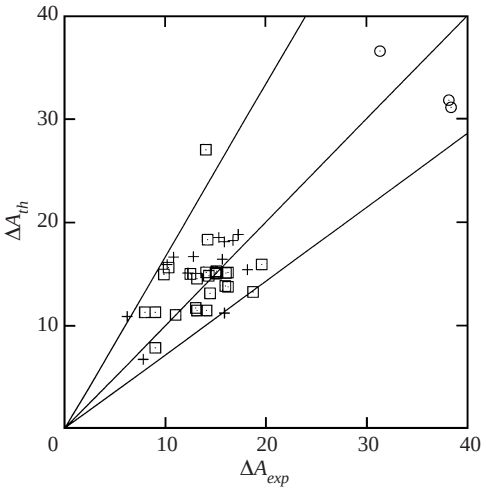


FIGURE 14. The difference between maximum and minimum bed elevation within a wavelength as predicted by theory ($\Delta A_{th}$) is compared with the experimental data ($\Delta A_{exp}$) (values in mm). Solid lines include the region where the relative error does not exceed 40%. +, $\lambda_b = 0.5$, $\delta = 0.125$; ⊡, $\lambda_b = 0.3$, $\delta = 0.125$; ⊙, $\lambda_b = 0.3$, $\delta = 0.25$.

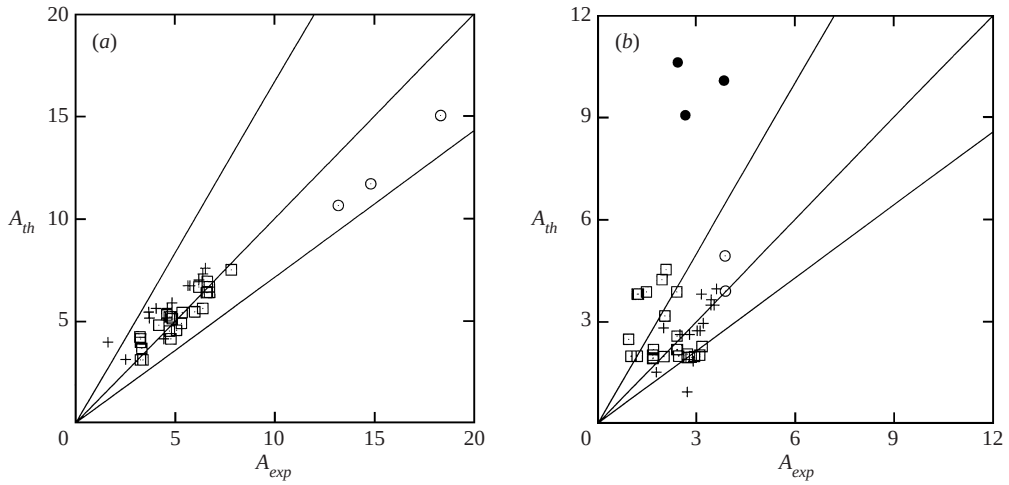


FIGURE 15. Comparison between theoretical predictions ($A_{th}$) and experimental values ($A_{exp}$) of the amplitude of the leading components of the Fourier representation of bed topography: (*a*) transverse mode '0'; (*b*) transverse mode '1' (values in mm). Solid lines include the region where the relative error does not exceed 40%. +, $\lambda_b = 0.5$, $\delta = 0.125$; ⊡, $\lambda_b = 0.3$, $\delta = 0.125$; ⊙, $\lambda_b = 0.3$, $\delta = 0.25$; ●, resonant values.

(theoretical predictions falling within the resonant range are denoted with the symbol '●' in figure 15*b*). In this case a linear approach is no longer valid and a nonlinear analysis is required, like that proposed by Seminara & Tubino (1992) for meandering channels. In figures 18(*a*) and 18(*b*), examples of predicted and observed values of the amplitude of the first three transverse harmonics of the Fourier representation of the bed profile are reported, in the case of non-resonant and resonant conditions, respectively.

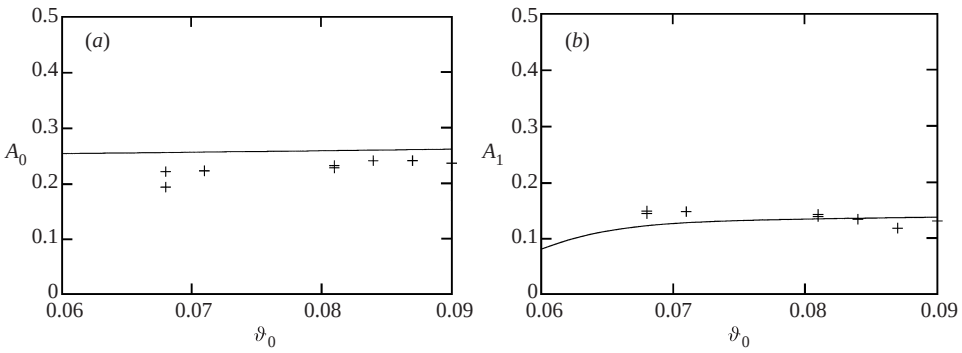


FIGURE 16. The dimensionless amplitude of the leading transverse modes of the Fourier representation of bed topography (scaled with $D_0^*$) is plotted versus the Shields parameter. Theory in continuous lines, experiments in crosses: initial slope $S = 0.007$, $\lambda_b = 0.5$, $\delta = 0.125$. (*a*) transverse mode '0'; (*b*) transverse mode '1'.

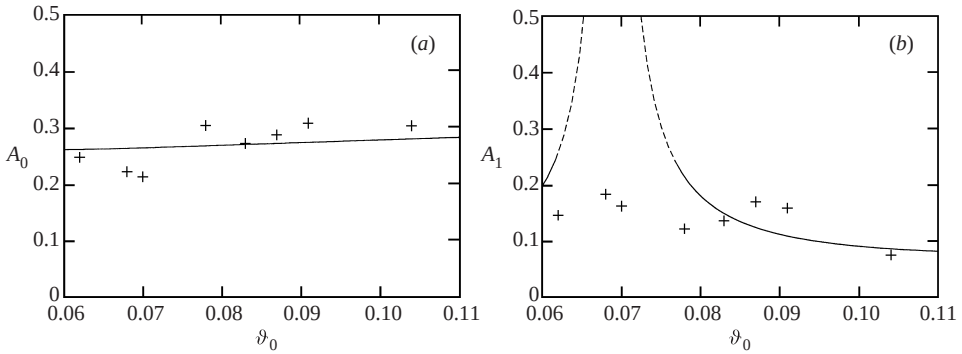


FIGURE 17. The dimensionless amplitude of the leading transverse modes of the Fourier representation of bed topography (scaled with $D_0^*$) is plotted versus the Shields parameter. Theory in continuous lines, experiments in crosses: initial bed slope $S = 0.01$, $\lambda_b = 0.3$, $\delta = 0.125$. (*a*) transverse mode '0'; (*b*) transverse mode '1'. The dashed line indicates the resonant range.

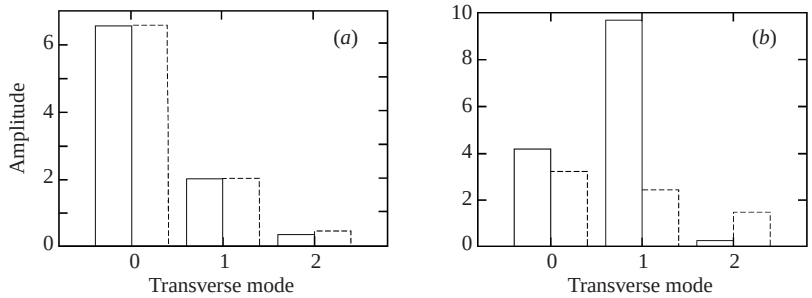


FIGURE 18. Comparison between theoretical predictions (continuous line) and experimental results (dashed lines) for the amplitude of the leading transverse modes of the Fourier representation of bed topography: (*a*) run 'b53'; (*b*) run 'b37' – resonant conditions (values in mm).

A detailed comparison between theoretical and experimental results for the whole set of experimental data is given in Repetto (2000).

It must be noted that the agreement between theoretical predictions and experimental values is less satisfactory close to the critical conditions for sediment movement

(as indicated in tables 1, 2 and 3, experimental data with $\vartheta_0 < 0.06$ are not included in the comparison). However, in the latter case the flume was often partially transporting sediment and emergence of bars occurred frequently; under these conditions the theory is not likely to be applicable. Furthermore, the damping effect of the planform on migrating alternate bars is weaker at low values of the Shields parameter. Hence, under these conditions the transverse structure of bottom configuration is affected by nonlinear interactions between free (alternate) and forced (central) bedforms whose effect is not included in the present analysis.

## 6. Correction due to streamline curvature effect on transverse bed shear stress

In this section we correct the two-dimensional model formulated in § 2 to take into account the effect of streamline curvature on transverse bottom shear stress.

The local radius of curvature $r_c$ of streamlines of depth-averaged flow is defined by the following equation:

$$\frac{1}{r_c} = \frac{-(V/U)_{,x}}{[1+(V/U)^2]^{3/2}}. \tag{6.1}$$

We pursue an approach originally introduced by Kalkwijk & de Vriend (1980) and further employed by Struiksma *et al.* (1985). The idea is to introduce an additive helical contribution to the transverse depth-averaged velocity, with vanishing net flux, orthogonal to the local depth-averaged velocity vector. The intensity of this contribution, which is associated with secondary flows, scales with the local ratio of flow depth to radius of streamline curvature. The suitability of the above approach has been demonstrated by Johannesson & Parker (1989) who showed that, for typical natural channels, the equations governing the problem for the depth-averaged transverse velocity and the additional helical contribution are not directly coupled to each other, at least within a linear context, the helical component being essentially driven by curvature. To characterize the vertical structure and the phase lag required for the secondary flow to adapt to spatial variations of streamline curvature, we follow the approach proposed by Tubino & Seminara (1990) for the case of meandering channels. The decomposition of transverse velocity implies the appearance of an additional term into the transverse bed shear stress component.

At the linear level, and in the presence of periodic variations of streamline curvature, the transverse component of the Shields stress can be written in the form

$$\tau_y = \tau'_y + \tau''_y = C_{f0} V_1 \left(1 - k\frac{\mathrm{i}\lambda_b}{\beta}\right), \tag{6.2}$$

where $\tau'_y$ is the contribution associated with the depth-averaged velocity and $\tau''_y$ accounts for curvature effects. The complex coefficient $k$ can be obtained from the three-dimensional model and coincides with the coefficient $k_4$ of Tubino & Seminara (1990) (see figure 4*d*).

In (2.13*a–d*), all the coefficients remain unchanged except for $a_4$ and $a_8$ which take the following expressions:

$$a_4 = \mathrm{i}\lambda_b + \beta C_{f0}\left(1 + \frac{\mathrm{i}\lambda_b k}{\beta}\right), \quad a_8 = 1 + \frac{\mathrm{i}\lambda_b k}{\beta}. \tag{6.3a,b}$$

Figures 19(*a*) and 19(*b*) show the amplitude and phase of the transverse mode '1' of the Fourier representation of bed elevation and of longitudinal depth-averaged

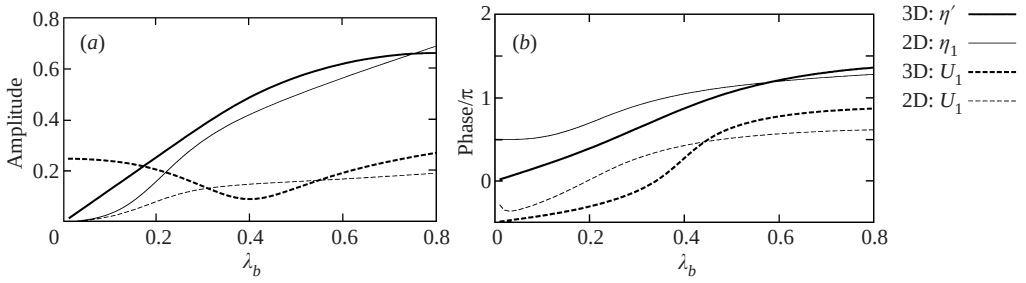


FIGURE 19. (*a*) The amplitude, and (*b*) the phase with respect to bank profile of transverse mode '1' of bed elevation and of longitudinal velocity obtained through the modified two-dimensional model (§ 6) are compared with the results of the three-dimensional model: $\beta = 10$, $\vartheta_0 = 0.1$, $d_s = 0.05$.

velocity as predicted by the three-dimensional and the corrected two-dimensional models. The results appear fairly close; with the inclusion of the effect of streamline curvature the two-dimensional model can describe the observed transverse variation of bed profile and flow characteristics. Furthermore, the dependence of the phase shift and amplitude of flow and bed variables on wavenumber of width variations is similar to that predicted by the three-dimensional model.

The remaining disagreement between the two formulations indicates that streamline curvature is not the only three-dimensional effect responsible for transverse variations of flow field and bed topography. In particular, the amplitude of transverse mode '1' of the longitudinal velocity component depends on $\lambda_b$ somewhat differently in the two models (figure 19*a*). This suggests that the longitudinal velocity is also influenced by secondary flow associated with convective terms, as discussed in § 3.

## 7. Stability of the planform

As pointed out in § 1, channel bifurcation can be viewed as the most important unit process which controls the production of new channels in braided rivers.

We now investigate how the results obtained through the present three-dimensional model can be used to set the basis of a simple model of bank stability able to predict the initial tendency of planform evolution. To this end we follow the simplified approach originally introduced for meandering channels by Ikeda, Parker & Sawai (1981), and further employed by Blondeaux & Seminara (1985), whereby bank erosion was related to the excess depth-averaged longitudinal velocity at the bank induced by flow perturbations which arise as a consequence of spatial variations of channel curvature. Here we investigate the conditions under which the perturbed flow induced by periodic width variations tends to enhance the given initial (small) perturbation of channel width.

The bank erosion model assumes that the channel is laterally stable in the absence of the forcing effect due to the variable width. The experimental observations of Ashmore (1982) provide some support to the above hypothesis in that single channels of braided networks reproduced in the laboratory were often found to attain quasi-equilibrium width conditions as defined by Parker (1978). Also notice that the transition to a central bar configuration, which eventually leads to flow bifurcation, is likely to occur in a channel which has undergone a relatively fast widening in the initial stage of the process and whose planform has been reworked by the migration of alternate bars.

Following Ikeda *et al.* (1981) we then assume the rate of bank retreat to be related

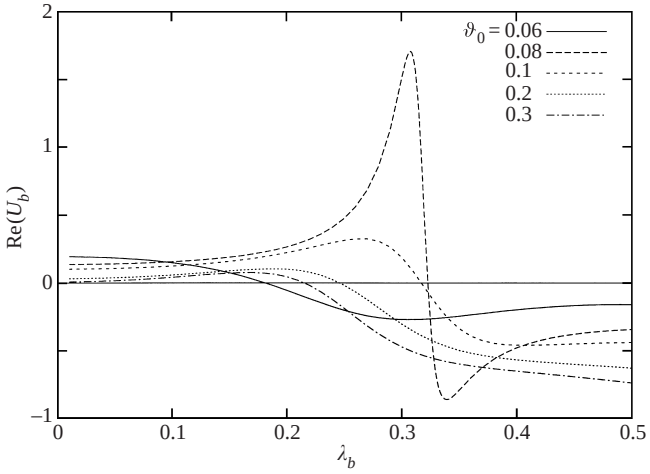


FIGURE 20. The real part of the perturbation of depth-averaged longitudinal velocity at the bank $U_b$ is plotted versus the wavenumber of width variations for different values of the Shields stress: $\beta = 15, d_s = 0.1$.

to the excess of depth-averaged velocity at the banks $U_b$, with respect to the uniform flow velocity, in the form

$$\frac{\mathrm{d}y_s}{\mathrm{d}t} = EU_b \exp(\mathrm{i}\lambda_b x) + \text{c.c.}, \tag{7.1}$$

where $y_s$ is the bank profile and $E$ is a suitable erosion coefficient. In spite of the approximate character of the model, which ignores several complicating features such as the effect of cohesion and vegetation, equation (7.1) has been employed successfully to predict the planimetric development of single thread meandering channels (see Seminara *et al.* 2001). The use of more refined bank erosion models (e.g. Osman & Thorne 1988; Hasegawa 1989; Mosselman 1989) is likely to affect our results only quantitatively. Also notice that the model can provide an estimate only of the initial tendency of planform development since the full coupling between bed and bank evolution is not taken into account (a recent attempt to account for the effect of a spatially uniform width changing in time is due to Darby & Thorne 1996).

According to (2.1*a*) the origin of the longitudinal axis coincides with the widest section. Hence, from (7.1) we readily find that the amplification rate of the bank profile is proportional to the real part of $U_b$, such that positive values of the latter quantity imply that bank erosion tends to widen the channel where it is wider than the average. Plots of the real part of $U_b$ for different values of the Shields stress are given in figure 20. It appears that the amplification rate is larger at relatively low values of Shields stress, with maximum values which typically occur in the range $\vartheta_0 = 0.07 \div 0.09$. As $\vartheta_0$ increases, the real part of $U_b$ may become negative, which implies that width variations are no longer destabilizing.

It is worth noting that the results reported in §§ 2 and 3 suggest that the conditions under which the perturbed flow induced by width variations produces an excess (positive) erosion rate at the widest section, implying incipient bifurcation of the flow, are strictly connected with the role of the transverse deformations of flow and bottom topography associated with three-dimensional effects. This is also shown in figure 21 where the phase $\alpha_u$ of the longitudinal depth-average velocity ($\alpha_u$ being the location of its maximum longitudinal value with respect to the bank profile) is

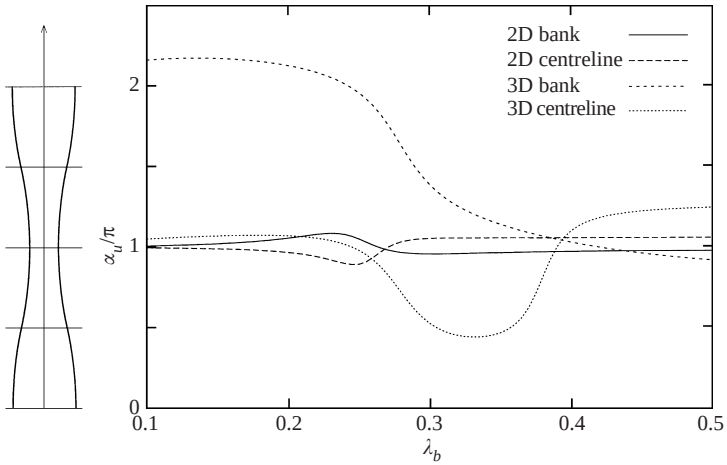


FIGURE 21. The phase $\alpha_u$ of the longitudinal depth-averaged velocity at the centreline and at the banks is plotted versus the wavenumber of width variations. Comparison between the results of two-dimensional and three-dimensional models: $\beta = 20$, $\vartheta_0 = 0.1$, $d_s = 0.05$.

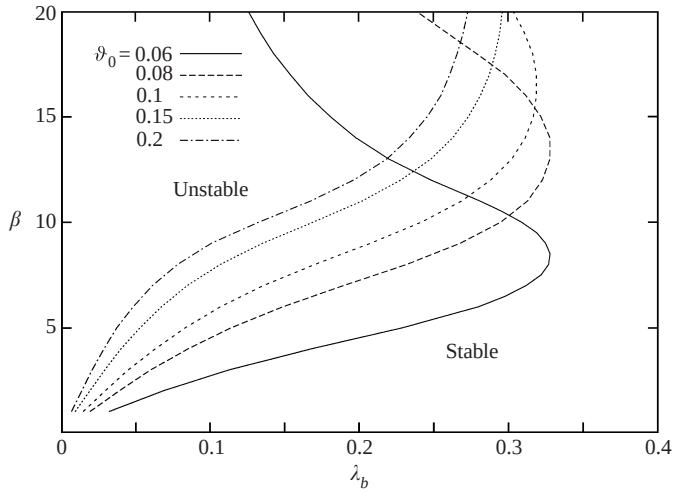


FIGURE 22. Neutral stability curves in the $(\lambda_b, \beta)$-plane for different values of the Shields parameter $\vartheta_0$ ($d_s = 0.1$).

plotted versus the wavenumber of width variations, for given values of the relevant dimensionless parameters. In the same figure results of the two-dimensional model (2D) are also shown. According to the above discussion the channel is planimetrically unstable when ($\alpha_u$) falls within the first or the fourth quadrant. It appears that while at the centreline the longitudinal velocity attains its maximum value within the narrow sections ($0.5 < \alpha_u/\pi < 1.5$), the opposite behaviour occurs at the banks where, for a relatively wide range of values of $\lambda_b$, the maximum longitudinal velocity is located at the wide sections ($\alpha_u/\pi > 1.5$). The figure also shows that according to the results of the two-dimensional model, the channel would be invariably stable, since the longitudinal velocity attains its maximum value close to the narrowest section both at the centreline and at the banks ($\alpha_u/\pi \sim 1$).

The region of instability widens for decreasing values of the Shields parameter

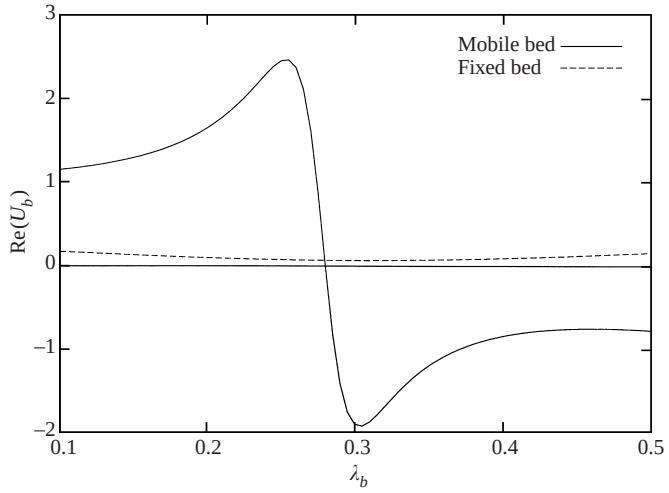


FIGURE 23. The amplification rate is plotted versus the wavenumber of width variations in the case of fixed bed (dashed line) and mobile bed (continuous line): $\beta = 20$, $\vartheta_0 = 0.1$, $d_s = 0.05$.

$\vartheta_0$, as shown in figure 22 where marginal stability curves in the $(\lambda_b, \beta)$-plane are reported for different values of the Shields parameter $\vartheta_0$ and a given value of the roughness parameter $d_s$. Also notice that for a given value of the Shields parameter the channel becomes unstable as the width ratio increases. The above results agree almost qualitatively with the experimental findings of Ashmore (1982, 1991). In fact, they suggest that the planimetric forcing induced by width variations, which may lead to the transition to a steady central bar pattern and to the incipient bifurcation of the channel, is more likely to operate in relatively wide channels at low Shields stress; the latter condition is gradually reached during the evolution process of laterally unconstrained cohesionless channels which start from a straight configuration. According to the results of our theory, the latter process can be traced following a line in the $(\beta, \vartheta_0)$-plane which moves from the stable to the unstable region in which width variations may become effective in shaping bed topography. Present theory suggests that, with $\beta$ typically ranging between 5 and 15, the destabilizing effect peaks at low values of Shields stress, a range physically sensible for gravel-bed braided rivers (e.g. Paola, Heller & Angevine 1992).

From figure 22 it also appears that the stability of the channel strongly depends on the wavenumber of width variations, such that for given values of $\beta$ and $\vartheta_0$ a threshold value of $\lambda_b$ exists above which the channel is stable. The latter dependence is mainly related to topographically driven effects on the flow field. This is shown in figure 23 where a comparison is shown between theoretical predictions of the real part of $U_b$ in the case of mobile and fixed beds. It appears that even in the case of a fixed bed, three-dimensional effects may be able to counteract the overall decrease of cross-sectionally averaged velocity which occurs in the widest section, leading to positive values of the amplification rate. However, the planimetric instability is strongly enhanced by flow divergence which is associated with the formation of a central bar in the wider part of the channel. As $\lambda_b$ increases, the central bar is progressively shifted downstream with respect to the bank profile, which implies that the topographic effects are no longer destabilizing.

## 8. Conclusions

The role of channel curvature in producing forced bar forms is well known; here we have demonstrated the analogous effect of width variations in forcing central bars and associated channel scours. The development of these bar-scour couplets is as central to river braiding as the development of curvature-induced bars is to river meandering. The two processes display strong similarities. The forcing effect of periodic width variations considered herein can be viewed as the symmetrical counterpart of the case of the periodic variation of curvature in meandering channels. In both cases three-dimensional effects and curvature-driven secondary flow appear to play comparable critical roles. Furthermore, an analogous resonant behaviour is exhibited by the theoretical solution in a given range of values of the relevant dimensionless parameters, when the external forcing excites quasi-steady natural responses of the unforced configuration (a straight channel with constant width). However, while in the case of meandering channels the forced response displays a spatial structure similar to that of alternate bars which would spontaneously develop in the channel, central bars are not expected to form spontaneously in the absence of some forcing mechanism, unless the channel is fairly wide. Coupled with a simple model for bank erosion, the present theory suggests that channel instability which may lead to incipient bifurcation of the flow is enhanced as the Shields stress decreases and the width ratio of the channel increases, in agreement with experimental observations.

Various limitations of the present model require further attention. In particular, to build a sound dynamical model of braided rivers the full coupling between bed and bank development would be required and finite-amplitude gravitational effects on transport rate should be accounted for.

This work has been jointly supported by the Italian Ministry for Scientific Research (MURST) and the University of Trento, under the project 'Fluvial and Coastal Morphodynamics' as well as by the US National Science Foundation.

## Appendix A. Solution of the differential problem (3.8a)

First, we determine the variable $\mathscr{G}_0(\zeta)$ in the form

$$\mathscr{G}_0 = \mathscr{G}_{0\hat{h}}(\zeta)\hat{h}, \tag{A 1}$$

solving the ordinary differential problem

$$\mathscr{L}_{\mathscr{G}}(\mathscr{G}_0) = \frac{2\hat{h}}{\beta F_0^2 \sqrt{C_{f0}}\mathscr{N}}, \tag{A 2a}$$

$$\mathscr{G}_{0,\zeta\zeta} = 0 \quad (\zeta = 1), \tag{A 2b}$$

$$\mathscr{G}_{0,\zeta} = 0 \quad (\zeta = z_0), \tag{A 2c}$$

$$\mathscr{G}_0 = 0 \quad (\zeta = z_0), \tag{A 2d}$$

where

$$\mathscr{L}_{\mathscr{G}}(\mathscr{G}) = \frac{\mathrm{d}^3\mathscr{G}}{\mathrm{d}\zeta^3} + \frac{1}{\mathscr{N}}\frac{\mathrm{d}\mathscr{N}}{\mathrm{d}\zeta}\frac{\mathrm{d}^2\mathscr{G}}{\mathrm{d}\zeta^2} - \frac{\mathrm{i}\lambda_b u_0}{\beta\sqrt{C_{f0}}\mathscr{N}}\frac{\mathrm{d}\mathscr{G}}{\mathrm{d}\zeta}. \tag{A 3}$$

We then determine $\hat{\mathscr{F}}$ from the following differential problem:

$$\mathscr{L}_{\mathscr{F}} = \Delta(\hat{h}, \hat{d}), \tag{A 4a}$$

$$\hat{\mathscr{F}}_{,\zeta\zeta} = 0 \quad (\zeta = 1), \tag{A 4b}$$

$$\hat{\mathscr{F}}_{,\zeta} = 0 \quad (\zeta = z_0), \tag{A 4c}$$

$$\hat{\mathscr{F}} = 0 \quad (\zeta = z_0), \tag{A 4d}$$

where

$$\mathscr{L}_{\mathscr{F}}(\mathscr{F}) = \mathscr{L}_{\mathscr{G}}(\mathscr{F}) + \frac{\mathrm{i}\lambda_b}{\beta\sqrt{C_{f0}}\mathscr{N}}\frac{\mathrm{d}u_0}{\mathrm{d}\zeta}\mathscr{F} - \frac{\sqrt{C_{f0}}}{\mathscr{N}}\mathscr{F}(1) \tag{A 5}$$

and

$$\Delta(x_1, x_2) = \frac{\mathrm{i}\lambda_b}{\beta F_0^2\sqrt{C_{f0}}\mathscr{N}}x_1 + \left[\frac{\sqrt{C_{f0}}}{\mathscr{N}}\left(\frac{C_D}{2} - 1\right) - \frac{\mathrm{i}\lambda_b}{\beta\sqrt{C_{f0}}\mathscr{N}}\frac{\mathrm{d}u_0}{\mathrm{d}\zeta}\int_{z_0}^{\zeta} u_0 \mathrm{d}\zeta\right] x_2. \tag{A 6}$$

Hence, we obtain

$$\hat{\mathscr{F}} = \hat{\mathscr{F}}_{\hat{h}}(\zeta)\hat{h} + \hat{\mathscr{F}}_{\hat{d}}(\zeta)\hat{d}. \tag{A 7}$$

The differential problem for $\mathscr{F}_0$ is

$$\mathscr{L}_{\mathscr{F}}(\mathscr{L}_0) = \Delta(h_0, d_0) - \frac{\hat{h}}{\beta\sqrt{C_{f0}}\mathscr{N}}\frac{\mathrm{d}u_0}{\mathrm{d}\zeta}\mathscr{G}_{0\hat{h}}, \tag{A 8a}$$

$$\mathscr{F}_{0,\zeta\zeta} = 0 \quad (\zeta = 1), \tag{A 8b}$$

$$\mathscr{F}_{0,\zeta} = 0 \quad (\zeta = z_0), \tag{A 8c}$$

$$\mathscr{F}_0 = 0 \quad (\zeta = z_0), \tag{A 8d}$$

with $\Delta$ given by (A 6). Hence, $\mathscr{F}_0$ can be written in the form

$$\mathscr{F}_0 = \mathscr{F}_{0h}(\zeta)h_0 + \mathscr{F}_{0d}(\zeta)d_0 + \hat{\mathscr{F}}_{0\hat{h}}(\zeta)\hat{h}. \tag{A 9}$$

Furthermore, $\mathscr{G}_m$ and $\mathscr{F}_m$ ($m = 1, 2, \ldots$) can be found in terms of $h_m$ and $d_m$ in the form

$$\mathscr{G}_m = \mathscr{G}_{mh}(\zeta)h_m, \tag{A 10a}$$

$$\mathscr{F}_m = \mathscr{F}_{mh}(\zeta)h_m + \mathscr{F}_{md}(\zeta)d_m, \tag{A 10b}$$

through the solution of the following differential system:

$$\mathscr{L}_{\mathscr{G}}(\mathscr{G}_m) = -\frac{m\pi h_m}{\beta F_0^2\sqrt{C_{f0}}\mathscr{N}}, \tag{A 11a}$$

$$\mathscr{L}_{\mathscr{F}}(\mathscr{F}_m) = \Delta(h_m, d_m) - \frac{m\pi}{\beta\sqrt{C_{f0}}\mathscr{N}}\frac{\mathrm{d}u_0}{\mathrm{d}\zeta}\mathscr{G}_m, \tag{A 11b}$$

$$\mathscr{G}_{m,\zeta\zeta} = 0 \quad (\zeta = 1), \tag{A 11c}$$

$$\mathscr{G}_{m,\zeta} = 0 \quad (\zeta = z_0), \tag{A 11d}$$

$$\mathscr{G}_m = 0 \quad (\zeta = z_0), \tag{A 11e}$$

$$\mathscr{F}_{m,\zeta\zeta} = 0 \quad (\zeta = 1), \tag{A 11f}$$

$$\mathscr{F}_{m,\zeta} = 0 \quad (\zeta = z_0), \tag{A 11g}$$

$$\mathscr{F}_m = 0 \quad (\zeta = z_0). \tag{A 11h}$$

Finally, the unknown constants $\hat{h}$, $\hat{d}$, $h_m$, $d_m$ ($m = 0, 1, 2, \ldots$) are determined through

the sidewall boundary conditions (3.19$a, b$) and (3.20$a, b$), the kinematic condition at the free surface (3.9$a$) and the Exner equation (3.12).

We first evaluate $\hat{h}$ from (3.19$a, b$), (3.21$a$) and (A 1) in the form

$$\hat{h} = \frac{\mathrm{i}\lambda}{\mathscr{G}_{0\hat{h}}(1)}. \tag{A12}$$

Notice that the contribution associated with $\mathscr{G}_m$ ($m \geqslant 1$) vanishes at the sidewall.

Substituting from (3.21$a, b$) into the boundary conditions (3.20$a, b$) leads to a relationship between $\hat{h}$ and $\hat{d}$ in the form

$$\hat{d} = \hat{h} + \frac{\beta\sqrt{\vartheta_0}}{2r}\left[\mathrm{i}\lambda_b - \left(\frac{\mathrm{d}^2\mathscr{G}_{0\hat{h}}/\mathrm{d}\zeta^2}{\mathrm{d}u_0/\mathrm{d}\zeta}\right)_{z_0}\right]. \tag{A13}$$

The kinematic condition (3.9$a$), where $w'$ has been substituted through (3.14), gives

$$\mathrm{i}\lambda_b[A_m(\hat{\mathscr{F}} + \hat{d}) + \mathscr{F}_m + d_m] + B_m\mathscr{G}_m = 0 \quad (\zeta = 1) \quad (m = 0, 1, 2, \ldots), \tag{A14}$$

where

$$B_0 = 1, \tag{A15a}$$

$$B_m = m\pi \quad (m > 0), \tag{A15b}$$

and $A_m$ are the coefficients of the Fourier representation of the function $y^2$ which are

$$A_0 = \frac{1}{3}, \tag{A16a}$$

$$A_m = \frac{4(-1)^m}{m^2\pi^2} \quad (m > 0). \tag{A16b}$$

From (A14), we then obtain a first relationship between the unknown coefficients $d_m$ and $h_m$, where $\mathscr{G}_0$, $\hat{\mathscr{F}}$, $\mathscr{F}_0$, $\mathscr{G}_m$, $\mathscr{F}_m$, $\hat{h}$ and $\hat{d}$ are given by equations (A 1), (A 7), (A 9), (A 10$a, b$), (A12) and (A13), respectively.

A further relationship between $h_m$ and $d_m$ ($m = 0, 1, 2, \ldots$) arises from the Exner equation (3.12). We obtain

$$\mathrm{i}\lambda_b\Phi_T\left\{\frac{1}{2}C_D(A_m\hat{d} + d_m) + A_m\hat{\mathscr{F}}(1) + \mathscr{F}_m(1) + \frac{1}{\sqrt{C_{f0}}}\left[\mathscr{N}\frac{\mathrm{d}^2}{\mathrm{d}\zeta^2}(A_m\hat{\mathscr{F}} + \mathscr{F}_m)\right]_{z_0}\right\}$$
$$+\frac{B_m}{\sqrt{C_{f0}}}\left(\mathscr{N}\frac{d^2\mathscr{G}_m}{\mathrm{d}\zeta^2}\right)_{z_0} - \frac{r}{\beta\sqrt{\vartheta_0}}[2(\hat{h} - \hat{d}) - m^2\pi^2(h_m - d_m)] = 0. \tag{A17}$$

## REFERENCES


Ashmore, P. E. 1982 Laboratory modelling of gravel bed stream morphology. *Earth Surf. Proc. Landforms* **7**, 201–225.

Ashmore, P. E. 1991 How do gravel-bed rivers braid? *Can. J. Sci.* **28**, 326–341.

Bittner, L. 1994 River bed response to channel width variation. Master thesis, University of Illinois.

Blondeaux, P. & Seminara, G. 1985 A unified bar-bend theory of river meanders. *J. Fluid Mech.* **157**, 449–470.

Bridge, J. S. & Gabel, S. L. 1992 Flow and sediment dynamics in a low sinuosity, braided river: Calamus River, Nebraska Sandhill. *Sedimentology* **39**, 125–142.

Colombini, M., Seminara, G. & Tubino, M. 1987 Finite-amplitude alternate bars. *J. Fluid Mech.* **181**, 213–232.

Darby, S. E. & Thorne, C. R. 1996 Numerical simulation of widening and bed deformation of straight sand-bed rivers. I: Model development. *J. Hydraul. Engng ASCE* **122**, 184–193.

Dean, R. B. 1974 *Aero. Rep. 74–11*, Imperial College, London.

Hasegawa, S. 1989 Studies on quantitative and qualitative prediction of meander channel shift. In *River Meandering* (ed. S. Ikeda & G. Parker). AGU Water Resources Monograph, vol. 12, pp. 215–235.

Ikeda, S. 1982 Lateral bedload transport on side slopes. *J. Hydraul. Engng ASCE* **108**, 1369–1373.

Ikeda, S., Parker, G. & Sawai, K. 1981 Bend theory of river meanders. Part 1. Linear development. *J. Fluid Mech.* **112**, 363–377.

Johannesson, H. & Parker, G. 1989 Linear theory of river meanders. In *River Meandering* (ed. S. Ikeda & G. Parker). AGU Water Resources Monograph, vol. 12, pp. 181–213.

Kalkwijk, J. P. & de Vriend, H. J. 1980 Computation of the flow in shallow river bends. *J. Hydraul. Res.* **18**, 327–342.

Kinoshita, R. & Miwa, H. 1974 River channel formation which prevents downstream translation of transverse bars. *Shinsabo* **94**, 12–17 (in Japanese).

Kovacs, A. & Parker, G. 1994 A new vectorial bedload formulation and its application to the time evolution of straight river channels. *J. Fluid Mech.* **267**, 153–183.

Leopold, L. B. & Wolman, G. 1957 River channel patterns: braiding, meandering and straight. *Phys. Hydr. Stud. Rivers* **14**, 283–300.

Mosley, M. P. 1976 An experimental study of channel confluences. *J. Geol.* **4**, 535–562.

Mosselman, E. 1989 Theoretical investigation on discharge-induced river bank erosion. *Commun. Hydraul. Delft University of Technology, Rep.* 3–89.

Osman, A. M. & Thorne, C. R. 1988 Riverbank stability analysis. I: Theory. *J. Hydraul. Engng ASCE* **114**, 134–150.

Paola, C., Heller, P. L. & Angevine, C. L. 1992 The large-scale dynamics of grain-size variation in alluvial basins, 1: Theory. *Basin Res.* **4**, 73–90.

Parker, G. 1978 Self-formed straight rivers with equilibrium banks and mobile bed. Part 2. The gravel river. *J. Fluid Mech.* **89**, 127–146.

Parker, G. 1990 Surface-based bedload transport relation for gravel rivers. *J. Hydraul. Res.* **20**, 417–436.

Parker, G., Seminara, G. & Solari, L. 2000 Bedload on arbitrarily sloping beds. Part 1: Failure of the Bagnold hypothesis. Part 2: Alternative entrainment formulation. *Water Resources Res.* (submitted).

Repetto, R. 2000 Unit processes in braided rivers. PhD thesis, University of Genova.

Seminara, G. 1995 Invitation to river morphodynamics. *Pitman Research Notes in Mathematics, 335* (ed. A. Doelman & A. van Harten), pp. 269–294. Longman.

Seminara, G. & Tubino, M. 1989 Alternate bars and meandering: free, forced and mixed interactions. In *River Meandering* (ed. S. Ikeda & G. Parker). AGU Water Resources Monograph, vol. 12, pp. 267–320.

Seminara, G. & Tubino, M. 1992 Weakly nonlinear theory of regular meanders. *J. Fluid Mech.* **244**, 257–288.

Seminara, G., Zolezzi, G., Tubino, M. & Zardi, D. 2001 Downstream and upstream influence in river meandering. Part 2. Planimetric development. *J. Fluid Mech.* **438**, 213–230.

Shimizu, Y. & Itakura, T. 1989 Calculation of bed variation in alluvial channels. *J. Hydraul. Engng ASCE* **115**, 367–384.

Struiksma, N., Olesen, K. W., Flokstra, C. & de Vriend, H. J. 1985 Bed deformation in curved alluvial channels. *J. Hydraul. Res.* **23**, 57–79.

Talmon, A. M., Struiksma, N. & Van Mierlo, M. C. L. M. 1995 Laboratory measurements of the direction of sediment transport on transverse alluvial-bed slopes. *J. Hydraul. Res.* **33**, 519–534.

Tubino, M. & Seminara, G. 1990 Free-forced interactions in developing meanders and suppression of free bars. *J. Fluid Mech.* **214**, 131–159.

Whiting, P. J. & Dietrich, W. E. 1993 Experimental studies of bed topography and flow patterns in large amplitude meanders. 1. Observations. *Water Resources Res.* **29**, 3605–3622.